

# Constraints from the Neutron EDM on Subleading Effective Operators for Direct Dark Matter Searches

---

Manuel Drees,<sup>a</sup> Rahul Mehra<sup>a,1</sup>

<sup>a</sup>*Bethe Center for Theoretical Physics and Physikalisches Institut, Universität Bonn, Nussallee 12, D-53115 Bonn, Germany*

*E-mail:* [drees@th.physik.uni-bonn.de](mailto:drees@th.physik.uni-bonn.de), [rmehra@physik.uni-bonn.de](mailto:rmehra@physik.uni-bonn.de)

ABSTRACT: Interactions between Dark Matter (DM) and nucleons relevant for direct search experiments can be organised in a model independent manner using a Galilean invariant, non-relativistic effective field theory (NREFT). Here one expands the interactions in powers of the momentum transfer  $\vec{q}$  and DM velocity  $\vec{v}$ . This approach generates many operators. The potentially most important subleading operators are odd under  $T$ , and can thus only be present in a theory with  $CP$  violating interactions. We consider two such operators, called  $\mathcal{O}_{10}$  and  $\mathcal{O}_{11}$  in the literature, in simplified models with neutral spin-0 mediators; the couplings are chosen such that the coefficient of the leading spin-independent (SI) operator, which survives for  $\vec{v} \rightarrow 0$ , vanishes at tree level. However, it is generically induced at the next order in perturbation theory. We perform a numerical comparison of the number of scattering events between interactions involving the  $T$ -odd operators and the corresponding loop induced SI contributions. We find that for “maximal”  $CP$  violation the former can dominate over the latter. However, in two of the three models we consider, an electric dipole moment of the neutron (nEDM) is induced at two-loop order. We find that the experimental bound on the nEDM typically leads to undetectably small rates induced by  $\mathcal{O}_{10}$ . On the other hand, the model leading to a nonvanishing coefficient of  $\mathcal{O}_{11}$  does not induce an nEDM.

---

<sup>1</sup>Corresponding author.

---

## Contents

<b>1</b>	<b>Introduction</b>	<b>1</b>
<b>2</b>	<b>NREFT and Simplified Models</b>	<b>4</b>
2.1	Model I	6
2.2	Model II	10
2.2.1	Model IIa	11
2.2.2	Model IIb	14
2.3	The Neutron EDM	16
<b>3</b>	<b>Results and Discussions</b>	<b>18</b>
<b>4</b>	<b>Summary and Conclusions</b>	<b>29</b>
<b>A</b>	<b>1-loop calculations</b>	<b>32</b>
A.1	Model I Matrix Element	32
A.1.1	Model I Loop Functions	34
A.2	Model IIa and IIb Matrix Elements	35
A.2.1	Model IIa and IIb Loop Functions	39
<b>B</b>	<b>2-Loop Calculations</b>	<b>42</b>

---

## 1 Introduction

The search for non-gravitational interactions of Dark Matter (DM) has not yielded a convincing signal so far. This is in stark contrast with the accumulated evidence for its gravitational interactions across a broad range of astrophysical length scales. Direct searches aim to detect non-gravitational interactions by observing the recoil of a target nucleus after an incoming DM particle has scattered off it. Terrestrial experiments using this search principle have led to tight constraints on the DM mass and cross-section parameter space [1–14]. For the past few decades such experimental efforts have focused on particle DM with weak scale interactions termed as Weakly Interacting Massive Particles (WIMPs). WIMPs can be produced in the early universe through freeze-out from the thermal plasma, which yields the observed DM relic abundance [15] for very roughly electroweak strength effective couplings. This has made WIMPs a particularly compelling category of DM candidates.

In order to interpret the results of direct search experiments one has to make assumptions regarding the nature of the interaction between DM and nucleons. Traditionally it was assumed that DM-nucleon interactions are dominated by just two operators describing spin independent (SI) and spin dependent (SD) interactions in the limit of zero WIMP velocity

[16]. These SI and SD operators are the leading terms of an EFT description, which is an expansion in powers of small parameters such as the DM velocity  $v$  and three momentum transfer scaled by the nucleon mass  $\vec{q}/m_N$ . Since  $v/c \lesssim \mathcal{O}(10^{-3})$  in the solar neighborhood, the momentum transfer is restricted to  $|\vec{q}| \lesssim \mathcal{O}(100 \text{ MeV})$ . Although the momentum exchange can be substantial on nuclear physics scales, it is far below the electroweak scale, and also below the range of WIMP masses most direct search experiments can probe. Hence, it is reasonable to expect that the canonical SI and SD interactions (zeroth order terms) dominate the EFT expansion.

A detailed non-relativistic effective field theory (NREFT) description of elastic DM–nucleus scattering retains NLO and NNLO terms by modeling the nucleus as a spatially extended composite particle with spin and charge densities [17–20]. For WIMPs of spins 0 or 1/2, truncating the EFT expansion at second order generates a total of 14 operators.<sup>1</sup> Since these higher order terms vanish for  $v \rightarrow 0$ , they lead to a spectrum of recoil energies quite different from the usual quasi-exponential fall-off, often preferring energies larger than the typical range of values implemented for SI and SD searches in experiments [23]. Multiple experiments have now extended their recoil energy search window in order to optimize the search strategy in the NREFT framework [24–33].

The NREFT contains, at least, 28 free parameters when the operators for neutrons and protons are counted separately. Probing this large parameter space is an arduous task. A number of global analyses using data from current and planned direct detection experiments have placed upper limits on the coupling strengths in this multi-dimensional parameter space [34–40]. A common conclusion drawn from these global analyses is that experiments are nearly as sensitive to some momentum- or velocity-dependent operators that are odd under  $P$  (parity) and  $T$  (time reversal) transformations as they are to the leading SD operator. These subleading operators have been scrutinized less in the literature. It is therefore interesting to study the phenomenology of models where they are generated in the non-relativistic (NR) limit, and to understand when these operators can dominate over the traditional SI and SD interactions.

The CPT theorem [41, 42] implies that every  $T$ -odd NREFT operator must arise from a  $CP$ -violating (CPV) quantum field theory, where  $C$  refers to charge conjugation. However, there are extremely stringent experimental constraints on  $CP$  violation [43], which can be used to place constraints on such NREFT operators. The electric dipole moment of the neutron (nEDM) is one such observable. The sensitivity of current experiments [44–46] is several orders of magnitude above the prediction of the standard model of particle physics (SM), but they provide tight constraints on flavor diagonal  $CP$  violation in extensions of the SM. The experimental upper limit on the nEDM is

$$|d_n| < 1.8 \times 10^{-26} \text{ e} \cdot \text{cm} \quad (90 \% \text{ C.L.}) . \quad (1.1)$$

There have been a number of articles linking extensions of the SM to low energy NREFT operators [47–49]. In particular, Ref. [47] lists a set of simplified models for scalar, spinorial and vector DM candidates and derives the full set of NREFT operators in terms of the

---

<sup>1</sup>The set of NREFT operators is substantially enlarged for WIMPs of higher spin [21, 22].

parameters for each simplified model. However, it is worth noting that most extensions of the SM only generate a small subset of the NREFT operators. Moreover, in most cases the leading order operators describing the SI and SD interactions are generated as well, and will then typically dominate. However, it is conceivable that the standard operators are strongly suppressed, in which case formally subleading operators actually provide the dominant contribution to scattering.

In Ref. [50], we considered simplified models with charged mediators, which are exchanged in the  $s$ -channel in DM-nucleon scattering. We found that suppressing the leading SI operator required finetuning of couplings; moreover, the bound on the nEDM, which is generated at one-loop in these models, implies that the subleading operators lead to undetectably small DM scattering rates. The  $P$ -odd,  $T$ -odd operators can thus be neglected in such scenarios.

In this article, we consider models that augment the SM by a WIMP candidate and a mediator particle which does not carry electric or color charge; DM-nucleon scattering then proceeds via  $t$ -channel diagrams. If one allows all couplings that respect the  $SU(3)_C \times U(1)_{\text{em}}$  gauge symmetry of the simplified Lagrangian, the leading SI term will be generated at tree level. However, the coefficient of this operator can be “switched off” by setting relevant coupling(s) to zero. This is an ad hoc choice, which cannot be justified by any symmetry. In this case, at the lowest order in perturbation theory, these models generate the  $P$ -odd,  $T$ -odd operators  $\mathcal{O}_{10}$  or  $\mathcal{O}_{11}$  without giving rise to the leading order operators. However, since the vanishing of the coefficient of the leading SI operator is not enforced by a symmetry, it will usually be generated at the next order in perturbation theory. Since now the contribution from the leading operator to DM-nucleon scattering is loop suppressed<sup>2</sup> while the contributions from  $\mathcal{O}_{10}$  and  $\mathcal{O}_{11}$  are suppressed by powers of  $v$  or  $|\vec{q}|/m_N$ , it is not a priori obvious which contribution is more important. We therefore numerically compare these contributions to the total number of events for a Xenon target. We find that for large regions in the parameter space of these models, the subleading  $P$ -odd,  $T$ -odd operators actually dominate over the SI term if the latter is purely loop-induced.

However, in models where tree level interactions generate only  $\mathcal{O}_{10}$ , we find that an nEDM is generically induced at two-loop order. The resulting upper bound on the couplings then again leads to unobservably small scattering rates, so that contributions from  $\mathcal{O}_{10}$  to DM-nucleon scattering can be neglected. On the other hand, in the model where  $\mathcal{O}_{11}$  is generated at tree level, the CP violation is restricted to the dark sector, and no nEDM is generated (apart from the tiny SM contribution). This case then provides an example of an NLO operator dominating over the traditional SI operator in DM-nucleon scattering, at least at the level of a simplified model.

The remainder of this article is organized as follows. In Section 2, we provide a brief introduction to the NREFT formalism, and introduce three  $CP$  violating simplified models

---

<sup>2</sup>For a purely pseudoscalar mediator, loop-induced contributions to  $\mathcal{O}_1$  typically dominate the DM scattering rate [51–54]. However, the mediator has to have both scalar and pseudoscalar couplings in order to generate  $\mathcal{O}_{10}$  or  $\mathcal{O}_{11}$ . A light mediator with general CP phases was considered in ref.[55], but constraints on these phases from EDMs were not considered, minimal flavor violation was assumed, and a trilinear coupling of the mediator to the SM Higgs boson was introduced.

yielding the  $P$ - and  $T$ -odd NREFT operators. We also compute the loop diagrams for WIMP–nucleon scattering that give rise to the leading SI operator in the non-relativistic limit. We then match the different scattering contributions to the corresponding four-field effective operators and finally match these to the set of NREFT operators. We also compute the two-loop Feynman diagrams that induce a nEDM and discuss the implications for the corresponding  $P$ -,  $T$ -odd operator in the NREFT. In Section 3 we compute the number of events for a Xenon target for the three simplified models. We discuss our main numerical results, comparing the contributions of the NREFT operators to elastic WIMP–nucleon scattering. We conclude in Section 4. Details of our loop computations are given in Appendices A and B.

## 2 NREFT and Simplified Models

A non-relativistic effective field theory (NREFT) of elastic scattering between DM and nuclei exhaustively categorizes the possible interactions involved in direct searches. An incoming DM particle striking a target nucleus on Earth is quite slow in the detector rest frame,  $v/c \sim \mathcal{O}(10^{-3})$ , and therefore a non-relativistic EFT can be used to describe the scattering. This simplifies the nuclear physics required to compute the scattering rate, which is nevertheless rather nontrivial [18]. Traditionally only the leading terms were kept, which remain finite as  $v \rightarrow 0$  [16]. The first and second order terms in DM velocity  $v$  and momentum transfer  $\vec{q}/m_N$  (in units of the nucleon mass) were considered only relatively recently [18–20, 49, 56]. In the following we briefly summarize the salient points.

In this NREFT elastic DM–nucleon scattering is described using a basis of operators constructed from the following Hermitian quantities invariant under Galilean transformations:

$$i\vec{q}, \quad \vec{v}^\perp \equiv \vec{v} + \frac{\vec{q}}{2\mu_N}, \quad \vec{S}_N, \quad \vec{S}_\chi. \quad (2.1)$$

Here  $\mu_N = m_N m_{\text{DM}} / (m_N + m_{\text{DM}})$  is the reduced mass of the DM–nucleon system. Energy conservation implies that the transverse velocity  $\vec{v}^\perp$  is orthogonal to the momentum transfer  $\vec{q}$ .  $\vec{S}_N$  and  $\vec{S}_\chi$  are the spin of the nucleon and the WIMP  $\chi$ ; of course, the latter may be zero. Using these four building blocks, and only imposing Galilean invariance, one obtains a set of linearly independent operators  $\mathcal{O}_i$  when the EFT is truncated at second order in the expansion parameter  $\vec{q}/m_N$ . Table 1 lists this set of 14 operators; the operators  $\mathcal{O}_1$  and  $\mathcal{O}_4$  describe the traditional leading SI and SD interaction, respectively. Note that the coefficients of these operators are in general different for neutrons and protons.

No invariance under any discrete symmetry was imposed in the construction of the NREFT operators. Their behavior under discrete transformations, in particular parity ( $P$ ) and time reversal ( $T$ ), can thus be used to classify the operators. A parity transformation corresponds to  $\vec{q} \rightarrow -\vec{q}$ ,  $\vec{v}^\perp \rightarrow -\vec{v}^\perp$ , while  $\vec{S}_N$  and  $\vec{S}_\chi$ , being pseudovectors, remain unchanged. On the other hand, under time reversal, all four vectors listed in (2.1) change sign, and in addition  $i \rightarrow -i$  (i.e. the Hermitian operator  $i\vec{q}$  remains unchanged). This leads to the following

$$\begin{aligned}
\mathcal{O}_1 &= 1_{\chi} 1_N; & \mathcal{O}_6 &= \left( \frac{\vec{q}}{m_N} \cdot \vec{S}_N \right) \left( \frac{\vec{q}}{m_N} \cdot \vec{S}_\chi \right); & \mathcal{O}_{10} &= i \frac{\vec{q}}{m_N} \cdot \vec{S}_N; \\
\mathcal{O}_3 &= i \vec{S}_N \cdot \left( \frac{\vec{q}}{m_N} \times \vec{v}^\perp \right); & \mathcal{O}_7 &= \vec{S}_N \cdot \vec{v}^\perp; & \mathcal{O}_{11} &= i \frac{\vec{q}}{m_N} \cdot \vec{S}_\chi; \\
\mathcal{O}_4 &= \vec{S}_\chi \cdot \vec{S}_N; & \mathcal{O}_8 &= \vec{S}_\chi \cdot \vec{v}^\perp; & \mathcal{O}_{12} &= \vec{S}_\chi \cdot (\vec{S}_N \times \vec{v}^\perp); \\
\mathcal{O}_5 &= i \vec{S}_\chi \cdot \left( \frac{\vec{q}}{m_N} \times \vec{v}^\perp \right); & \mathcal{O}_9 &= i \vec{S}_\chi \cdot \left( \vec{S}_N \times \frac{\vec{q}}{m_N} \right); & \mathcal{O}_{13} &= i (\vec{S}_\chi \cdot \vec{v}^\perp) \left( \frac{\vec{q}}{m_N} \cdot \vec{S}_N \right); \\
& & \mathcal{O}_{14} &= i (\vec{S}_N \cdot \vec{v}^\perp) \left( \frac{\vec{q}}{m_N} \cdot \vec{S}_\chi \right)
\end{aligned}$$

**Table 1:** List of operators in the NREFT for elastic WIMP–nucleon scattering. We adopt the conventions of [20] by defining the operators normalized by the nucleon mass  $m_N$  in order to have a dimensionless basis. We omit the invariant  $\mathcal{O}_2 = v_\perp^2$  because it is a second order correction to the SI operator  $\mathcal{O}_1$ , as well as  $\mathcal{O}_{15} = -\left(\vec{S}_\chi \cdot \frac{\vec{q}}{m_N}\right) \left((\vec{S}_N \times \vec{v}^\perp) \cdot \frac{\vec{q}}{m_N}\right)$  since it generates a cross section of order  $v_T^6$ , which is N<sup>3</sup>LO.

classification:

$$\begin{aligned}
\mathcal{O}_1, \mathcal{O}_3, \mathcal{O}_4, \mathcal{O}_5, \mathcal{O}_6 &: P\text{-even and } T\text{-even,} \\
\mathcal{O}_7, \mathcal{O}_8, \mathcal{O}_9 &: P\text{-odd and } T\text{-even,} \\
\mathcal{O}_{13}, \mathcal{O}_{14} &: P\text{-even and } T\text{-odd,} \\
\mathcal{O}_{10}, \mathcal{O}_{11}, \mathcal{O}_{12} &: P\text{-odd and } T\text{-odd.}
\end{aligned}$$

The  $P$  and  $T$  quantum numbers of the NREFT operators must match those of the relativistic operators generating them. In particular, the  $CPT$  theorem stipulates that only a  $CP$  violating quantum field theory with a DM candidate can yield any of the  $T$ -odd operators. Out of those, the operators  $\mathcal{O}_{12}$ ,  $\mathcal{O}_{13}$  and  $\mathcal{O}_{14}$  are not generated in scenarios with  $t$ -channel mediator with spin  $\leq 1$ ;<sup>3</sup> the latter two operators anyway contribute little to the scattering cross section if all operators have coefficients of similar size [39]. Therefore, we focus on  $\mathcal{O}_{10}$  and  $\mathcal{O}_{11}$  in the following.

Connecting a relativistic model for DM leading to specific DM–quark and/or DM–gluon interactions with the NREFT in general involves two steps. First, one integrates out the heavy mediator(s), where “heavy” here refers to all mediators  $\phi$  with mass  $m_\phi$  well above 100 MeV, which is the maximal three-momentum exchange in DM–nucleus scattering.<sup>4</sup> This results in relativistic but non-renormalizable four-field DM–quark and/or DM–gluon operators. In the second step one takes the non-relativistic limit of these four-field operators and matches them onto the NREFT operators listed in Table 1. This leads to an effective Lagrangian containing some (or all) of these operators, with coefficients determined by the couplings and masses of the original relativistic theory. The computation of DM–nucleus

<sup>3</sup> $\mathcal{O}_{12}$  can be generated in a model with a spin-1/2 WIMP and spin-0  $s$ -channel mediator, but the constraint from the nEDM forces this contribution to be negligible [50].

<sup>4</sup>In order to include light mediators in the NREFT the differential cross section should be multiplied with  $[m_\phi^2/(m_\phi^2 + \vec{q}^2)]^2$ ; this will lead to a softening of the recoil spectrum for  $\vec{q}^2 \gtrsim m_\phi^2$ .

scattering rates from these coefficients involves numerous nuclear “response functions”; we refer to ref.[20], whose expressions we used in our own numerical code.

As already mentioned, the NREFT is an expansion in powers of  $v$  or  $\vec{q}$ . If all coefficients in the NREFT are of comparable magnitude, the total scattering rate typically receives the largest contribution from the SI operator  $\mathcal{O}_1$ , which is of zeroth order in the expansion. Moreover, this contribution is enhanced by  $A^2$ , where  $A$  is the nucleon number. For large momentum exchange,  $|\vec{q}| \gtrsim 1/r_N$  where  $r_N$  is the radius of the target nucleus, the rate is somewhat suppressed by a form factor, but even without form factor this contribution to the scattering rate peaks at  $|\vec{q}| \rightarrow 0$ .

$\mathcal{O}_4$  is also of zeroth order in the expansion. However, since the spins of the nucleons largely cancel in any given nucleus, there is no  $A^2$  enhancement; in fact,  $\mathcal{O}_4$  does not contribute at all if the target nucleus has no spin.

As already noted, for sufficiently heavy DM particle (and target nucleus) the three-momentum exchange can reach  $|\vec{q}| \sim 100$  MeV. In this high momentum exchange region of phase space the operators that are linear in  $\vec{q}$  and independent of  $\vec{v}^\perp$  are therefore only suppressed by a factor  $\sim 0.1$ ; these are the operators  $\mathcal{O}_{10}$  and  $\mathcal{O}_{11}$  which are the focus of our study.<sup>5</sup> The contribution from  $\mathcal{O}_{11}$  is  $A^2$  enhanced, up to a form factor, but requires the DM particle to carry spin. The contribution from  $\mathcal{O}_{10}$  suffers similar cancellations as that from  $\mathcal{O}_4$ , but can survive even for scalar DM particle.

Naively the contributions of operators involving  $\vec{v}^\perp$  should be suppressed by a factor  $v^2 \sim 10^{-6}$ ; indeed, compared to the contribution from  $\mathcal{O}_1$  this is almost true. However, the richer structures can lead to nuclear response  $\propto \vec{S}_N \cdot \vec{L}_N$  [20],  $\vec{L}_N$  being the orbital angular momentum of a given nucleon; in this product the contributions of paired nucleons do *not* cancel. As a result, for heavy target nuclei and similar coefficients the contribution from  $\mathcal{O}_{12}$  often exceeds that from  $\mathcal{O}_4$  [39]; however, as already noted  $\mathcal{O}_{12}$  is not generated in the models with neutral mediator that we consider in this article. Similarly, for equal coefficients  $\mathcal{O}_3$  typically contributes almost as much as  $\mathcal{O}_{10}$  does [39], but  $\mathcal{O}_3$  is not generated in leading order when starting from a relativistic theory [47].  $\mathcal{O}_{10}$  and  $\mathcal{O}_{11}$  are therefore the potentially most important higher order NREFT operators that can be generated from a relativistic QFT.

After these preliminaries, we are ready to introduce the simplified models we consider in this analysis. Recall that, in the spirit of ref.[47], we only impose invariance under  $SU(3)_C \times U(1)_{\text{em}}$ , not under the complete gauge group of the SM.

## 2.1 Model I

Model I contains a complex spin-zero WIMP  $S$  and a real spin-zero mediator  $\phi$ ; both are gauge singlets. We assume that the WIMP is odd and the mediator and all the SM particles are even under a new discrete symmetry  $\mathbb{Z}_2$ . This forbids dark matter decay, but allows  $\phi$  to couple to both  $S$  and to SM quarks  $q$ . The most general gauge invariant Lagrangian

---

<sup>5</sup>However, simplified models yielding  $\mathcal{O}_{11}$  in the non-relativistic limit always seem to result in the coefficient  $c_{11}$  containing an extra factor  $m_N/m_{\text{DM}}$  [47–50]; see also eq.(2.21) below. A discussion assuming  $m_{\text{DM}}$  independent Wilson coefficients therefore overestimates the importance of  $\mathcal{O}_{11}$ . Even with this caveat,  $\mathcal{O}_{11}$  remains the potentially most important non-leading NREFT operator for  $m_{\text{DM}} \lesssim 100$  GeV.

respecting the new  $\mathbb{Z}_2$  symmetry and keeping the real and imaginary parts of  $S$  degenerate thus is:<sup>6</sup>

$$\begin{aligned} \mathcal{L}^I = & (\partial_\mu S)^\dagger (\partial^\mu S) - m_S^2 S^\dagger S - \frac{\lambda_S}{2} (S^\dagger S)^2 + \frac{1}{2} \partial_\mu \phi \partial^\mu \phi - \frac{1}{2} m_\phi^2 \phi^2 - \frac{m_\phi \mu_1}{3} \phi^3 - \frac{\mu_2}{4} \phi^4 \\ & - g_1 m_S S^\dagger S \phi - \frac{g_2}{2} S^\dagger S \phi^2 - h_1^{ij} \phi \bar{q}_i q_j - i h_2^{ij} \phi \bar{q}_i \gamma^5 q_j . \end{aligned} \quad (2.2)$$

$U(1)_{\text{em}}$  invariance implies that the mediator  $\phi$  can only couple to quarks with identical electric charge. Hence the quark flavor indices  $i$  and  $j$  in the Yukawa coupling matrices are restricted to the same quark type. However, non-vanishing couplings of the mediator to quarks of different generations generate flavor changing neutral currents (FCNC) processes at tree level. Experimental constraints arising from meson mixing along with rare flavor changing decays severely limit these flavor non-diagonal couplings. Therefore we assume that the Yukawa coupling matrices in eq.(2.2) are diagonal in flavor space, in particular  $h_{1,2}^q \equiv h_{1,2}^{ii}$  where  $q$  denotes the quark flavor the mediator couples to.

In eq.(2.2) we have allowed both scalar and pseudoscalar couplings of  $\phi$  to the SM quarks. However, if  $g_1 h_1^q \neq 0$  there will be tree level contributions to  $\mathcal{O}_1$ , which will then completely dominate WIMP–nucleus scattering, in which case the nonleading operators in the NREFT would not need to be considered. Moreover,  $h_1^q h_2^q \neq 0$  for any quark  $q$  would yield an electric dipole moment of that quark at one-loop order, leading to very strong constraints on the parameters of the model. We therefore impose

$$h_1^q = 0 \quad \forall q . \quad (2.3)$$

We emphasize that this is completely ad hoc but necessary for considering the non-leading operators in the NREFT. In particular, it cannot be justified by any symmetry. In contrast, the requirement  $h_2^q = 0$ , which would also remove the EDMs but allow  $\mathcal{O}_1$ , could be justified by demanding  $CP$  conservation. Nevertheless “switching off”  $\mathcal{O}_1$  via eq.(2.3) is still less inelegant than requiring specific relations between non-zero couplings, as we had to do in our earlier analysis of models with charged  $s$ –channel mediators [50]. On the other hand, since eq.(2.3) cannot be enforced by a symmetry, we can already anticipate that higher order contributions will generate an effective  $h_1^q$  or, more generally, lead to nonvanishing  $\mathcal{O}_1$ .

The matrix element for tree level  $t$ –channel scattering  $S(p_S) + q(p_q) \rightarrow S(p'_S) + q(p'_q)$  is given by

$$\mathcal{M}_{Sq \rightarrow Sq}^I = - \frac{h_2^q g_1 m_S}{q^2 - m_\phi^2} \bar{u}(p'_q) i \gamma^5 u(p_q) . \quad (2.4)$$

For  $|q^2| \ll m_\phi^2$  we can ignore the  $q^2$  term in the  $\phi$  propagator. The matrix element can then be matched on to a relativistic effective operator  $S^\dagger S \bar{q} i \gamma^5 q$ , which reduces to the operator  $\mathcal{O}_{10}$  in the non-relativistic limit.

For Model I, at the lowest order in perturbation theory, thus only the operator  $\mathcal{O}_{10}$  contributes to DM–nucleus scattering. However, at the next-to-leading order the one-loop

---

<sup>6</sup>Essentially identical results can be derived for a real spin-zero WIMP.



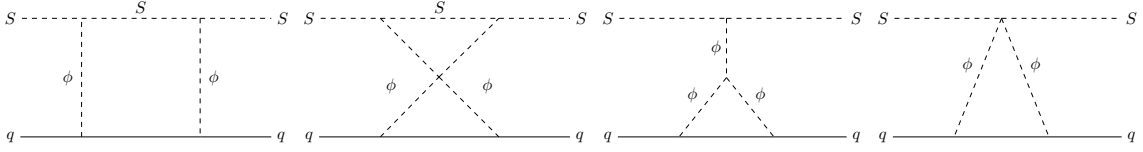


**Figure 1:** One-loop box and triangle Feynman diagrams in Model I which give contributions to  $\mathcal{O}_1$ .

Feynman diagrams shown in Fig. 1 can induce contributions from the operator  $\mathcal{O}_1$ . We use the Dirac equation and four-momentum conservation to write the resulting matrix elements in a form that is symmetric in DM momenta; see Appendix A.1 for details. The relativistic effective Lagrangian for Model I derived in this manner can be written as

$$\mathcal{L}_{\text{eff}}^{\text{I}} \supset c_{1,S}^{q,d5} S^\dagger S \bar{q}q + c_{10}^{q,d5} S^\dagger S \bar{q} i\gamma^5 q + c_{1,V}^{q,d6} i \left( S^\dagger \overleftrightarrow{\partial}_\mu S \right) \bar{q}\gamma^\mu q. \quad (2.5)$$

The Hermitean derivative on the complex scalars is defined as  $iS^\dagger \overleftrightarrow{\partial}_\mu S \equiv \frac{i}{2}(S^\dagger \partial_\mu S - S \partial_\mu S^\dagger)$ . The subscripts  $i$  on the quark-level Wilson coefficients  $c_i^{q,dj}$  ( $j = 5, 6$ ) denote the NREFT operator that the corresponding relativistic effective operator reduces; in case of  $\mathcal{O}_1$  we have distinguished the coefficient  $c_{1,S}$  of the product of two scalar currents from  $c_{1,V}$  which multiplies the product of two vector currents. Finally, the superscripts  $d5$  and  $d6$  refer to field operators with mass dimension 5 and 6, respectively.

Table 2 describes the matching of the relativistic effective operators onto the NREFT operators in terms of the parameters of Model I. The Wilson coefficients for the dimension-5 operators  $(S^\dagger S)(\bar{q}q)$  and  $(S^\dagger S)(\bar{q}i\gamma^5 q)$  have been divided by a factor of  $m_S$ , i.e. these are coefficients of the dimension-6 operators  $m_S(S^\dagger S)(\bar{q}q)$  and  $m_S(S^\dagger S)(\bar{q}i\gamma^5 q)$ ; this ensures that the expressions for all DM-nucleon cross sections contain the same factor  $\frac{\mu_{\chi N}^2}{\pi} (c_i^N)^2$  irrespective of the mass dimension of the relativistic operator involved. The loop functions  $M_i(r, s)$  and  $L_i(r)$  appearing in the box and triangle diagrams have been expressed as functions of dimensionless parameters  $r \equiv m_q/m_\phi$  and  $s \equiv m_S/m_\phi$ . Analytical expressions for these loop functions for Model I, and their  $m_q \rightarrow 0$  limits, can be found in Appendix A.1.1. The dimension-5 scalar-scalar operator  $(S^\dagger S)(\bar{q}q)$  as well as the dimension-6 vector-vector operator  $i \left( S^\dagger \overleftrightarrow{\partial}_\mu S \right) \bar{q}\gamma^\mu q$  both reduce to the leading order SI operator  $\mathcal{O}_1$  in the non-relativistic limit. Only the box diagrams give rise to both vector-vector and scalar-scalar relativistic operators, whereas the two triangle diagrams yield only the scalar-scalar operator. The first triangle diagram could be described in terms of an effective, loop-generated coupling  $h_1^q$ , thereby confirming our expectation that the choice  $h_1^q = 0$  is not technically natural; however, all four diagrams shown in Fig. 1 contribute at the same order in perturbation theory, and should therefore be included in a full NLO treatment. The loop-generated Wilson coefficients are all suppressed by the loop factor  $1/16\pi^2$  compared to the tree level diagram. The loop functions  $M_i$  have mass dimension  $-4$  while  $L_1$  has mass dimension  $-2$ , hence the quark-level Wilson coefficients  $c_i^q$  all have the same mass dimension  $-2$ . Since the scalar-scalar operator violates chirality, the contributions to  $c_{1,S}^{q,d5}$  are all  $\propto m_q$ .

	$S^\dagger \Gamma_S S \bar{q} \Gamma_q q$	$c_i^q$
Tree	$c_{10}^{q,d5} S^\dagger S \bar{q} i \gamma^5 q$	$\frac{h_2^q g_1}{m_\phi^2}$
Box	$c_{1,V,B}^{q,d6} i \left( S^\dagger \overleftrightarrow{\partial}_\mu S \right) \bar{q} \gamma^\mu q$	$\frac{(h_2^q)^2 g_1^2 m_S^2}{16\pi^2} M_1$
	$c_{1,S,B}^{q,d5} S^\dagger S \bar{q} q$	$\frac{(h_2^q)^2 g_1^2 m_S m_q}{16\pi^2} M_2$
Crossed	$c_{1,V,C}^{q,d6} i \left( S^\dagger \overleftrightarrow{\partial}_\mu S \right) \bar{q} \gamma^\mu q$	$-\frac{(h_2^q)^2 g_1^2 m_S^2}{16\pi^2} M_3$
Box	$c_{1,S,C}^{q,d5} S^\dagger S \bar{q} q$	$\frac{(h_2^q)^2 g_1^2 m_S m_q}{16\pi^2} M_4$
Triangle 1	$c_{1,S,T1}^{q,d5} S^\dagger S \bar{q} q$	$\frac{(h_2^q)^2 g_1 \mu_1 m_q}{16\pi^2 m_\phi} L_1$
Triangle 2	$c_{1,S,T2}^{q,d5} S^\dagger S \bar{q} q$	$-\frac{(h_2^q)^2 g_2 m_q}{16\pi^2 2m_S} L_1$

**Table 2:** Non-relativistic reduction of relativistic effective operators in Model I. The middle column gives the relativistic four-field operators that appear in the matrix element for WIMP–nucleon scattering. The right column gives the corresponding quark-level Wilson coefficient  $c_i^q$  of the relevant NREFT operators, where we have suppressed the dependence of the loop functions on dimensionless parameters, i.e.  $M_i \equiv M_i(r, s)$  and  $L_1 \equiv L_1(r)$  with  $r \equiv m_q/m_\phi$  and  $s \equiv m_S/m_\phi$ . The first line contributes to the coefficient of  $\mathcal{O}_{10}$ , all other lines describe contributions  $\propto \mathcal{O}_1$ .

The quark bilinears in eq.(2.5) and Table 2 must be promoted to nucleon bilinears in order to describe DM–nucleon scattering. The quark-level Wilson coefficients therefore have to be combined with corresponding nucleon embedding factors in order to derive the Wilson coefficients at the nucleonic level [18, 57]. Including contributions from the box and the triangle diagrams, the nucleonic Wilson coefficient  $c_1^N$  of the NREFT operator  $\mathcal{O}_1$  becomes:

$$\begin{aligned}
c_1^N|^{\text{I}} &= \frac{1}{16\pi^2} \left[ g_1^2 m_S^2 \left\{ \sum_{u,d} (h_2^q)^2 \mathcal{N}_q^N (M_1(r_q, s) - M_3(r_q, s)) \right\} \right. \\
&\quad + m_N \left( \sum_{u,d,s} (h_2^q)^2 f_{Tq}^N + \frac{2}{27} f_{TG}^N \sum_{c,b,t} (h_2^q)^2 \right) \\
&\quad \left. \times \left\{ g_1^2 m_S \left( M_2(r_q, s) + M_4(r_q, s) \right) + \left( \frac{g_1 \mu_1}{m_\phi} - \frac{g_2}{2m_S} \right) L_1(r_q) \right\} \right]. \quad (2.6)
\end{aligned}$$

Promoting the vector quark bilinear  $\mathcal{N}_q^N \equiv \langle \bar{N} | \bar{q} \gamma^\mu q | N \rangle$  to the vector nucleon bilinear yields the number of valence quarks of flavor  $q$  in the nucleon  $N$ , i.e.  $\mathcal{N}_u^p = \mathcal{N}_d^n = 2$ ,  $\mathcal{N}_d^p = \mathcal{N}_u^n = 1$ . The contribution of light quarks to the nucleon mass (scalar nucleon bilinear) is

given by

$$q = u, d, s : \langle \bar{N} | m_q \bar{q}q | N \rangle = m_N f_{Tq}^N. \quad (2.7)$$

The heavy quarks contribute to the nucleon mass via the trace anomaly of the energy–momentum tensor [58]:

$$q = c, b, t : \langle \bar{N} | m_q \bar{q}q | N \rangle = \frac{2}{27} m_N f_{TG}^N = \frac{2}{27} m_N \left( 1 - \sum_{q'=u,d,s} f_{Tq'}^N \right). \quad (2.8)$$

At first sight one might think that the contribution from the product of two vector currents dominates, since the corresponding nucleonic matrix elements  $\mathcal{N}_q^N$  are large. However, in the limit  $r_q \rightarrow 0$  the difference  $M_1(r_q, s) - M_3(r_q, s)$  vanishes  $\propto r_q^2$ . In contrast, the sum  $M_2(r_q, s) + M_4(r_q, s) \rightarrow 2M_2(0, s)$  remains finite for massless quarks. As a result, the first term in eq.(2.6) typically contributes much less than the remaining terms, which originate from the product of scalar currents.

For the tree–level scattering contribution reducing to  $\mathcal{O}_{10}$ , the nucleonic Wilson coefficient in the limit of vanishing momentum transfer is [18]

$$c_{10}^{N|I} = \frac{g_1}{m_\phi^2} \left( \sum_{u,d,s} h_2^q \Delta \tilde{q}^N - \Delta \tilde{G}^N \sum_{c,b,t} \frac{h_2^q}{m_q} \right) \quad (2.9)$$

where  $\Delta \tilde{q}^N$  and  $\Delta \tilde{G}^N$  are the light and heavy quark contributions to the nucleon level pseudoscalar bilinear, respectively. The latter hadronic matrix element is due to the QCD chiral anomaly:

$$q = c, b, t : \langle \bar{N} | \partial_\mu (\bar{q} \gamma^\mu \gamma^5 q) | N \rangle = 2m_q \langle \bar{N} | \bar{q} i \gamma^5 q | N \rangle + \frac{\alpha_s}{4\pi} \langle \bar{N} | G^{a\mu\nu} \tilde{G}_{\mu\nu}^a | N \rangle, \quad (2.10)$$

where  $G$  and  $\tilde{G}$  are the gluonic field strength tensor and its dual, respectively. The left–hand side can be set to zero since heavy quarks have no significant dynamics in the nucleon. Throughout our calculations, we take the numerical values of the coefficients that appear when quark bilinears are promoted to nucleon bilinears as given in the Appendix of Ref. [47].

## 2.2 Model II

In Model II we replace the complex scalar WIMP by a spin–1/2 gauge singlet Dirac fermion  $\chi$ , again using a real spin–zero mediator  $\phi$ . The couplings of the SM quarks  $q$  to the mediator are as in Model I. The WIMP  $\chi$  can also couple to the mediator  $\phi$  via a scalar ( $\lambda_1$ ) and a pseudoscalar coupling ( $\lambda_2$ ). The renormalizable  $SU(3)_C \times U(1)_{\text{em}}$  invariant Lagrangian is thus given by

$$\begin{aligned} \mathcal{L}^{\text{IIa}} = & i \bar{\chi} \not{D} \chi - m_\chi \bar{\chi} \chi + \frac{1}{2} \partial_\mu \phi \partial^\mu \phi - \frac{1}{2} m_\phi^2 \phi^2 + \frac{m_\phi \mu_1}{3} \phi^3 - \frac{\mu_2}{4} \phi^4 \\ & - \lambda_1 \phi \bar{\chi} \chi - i \lambda_2 \phi \bar{\chi} \gamma^5 \chi - h_1^{ij} \phi \bar{q}_i q_j - i h_2^{ij} \phi \bar{q}_i \gamma^5 q_j. \end{aligned} \quad (2.11)$$

We assume that the DM particle is odd and the SM particles along with the mediator are even under a new discrete  $\mathbb{Z}_2$  symmetry in order to prevent DM decay. In order to avoid

potentially very large new contributions to FCNC processes we again take flavor diagonal quark couplings, i.e.  $h_1^q \equiv h_1^{ij} \delta_{ij}$  and  $h_2^q \equiv h_2^{ij} \delta_{ij}$ .

If all Yukawa couplings (of a given flavor) appearing in the Lagrangian (2.11) are of similar magnitude, WIMP–nucleus scattering on heavy target nuclei will be completely dominated by a tree level contribution from  $\mathcal{O}_1$ , with coefficient  $\propto \lambda_1 h_1^q$ . We thus have to set at least one of these couplings to zero. On the other hand, setting both of them to zero would also “switch off” the operators  $\mathcal{O}_{10}$  and  $\mathcal{O}_{11}$  which we seek to generate. We thus consider two variants of Model II:

$$\begin{aligned} \text{Model IIa} : h_1^q &= 0 \quad \forall q; \\ \text{Model IIb} : \lambda_1 &= h_2^q = 0 \quad \forall q. \end{aligned} \quad (2.12)$$

Setting  $h_1^q \cdot h_2^q = 0$  again ensures that no electric dipole moments are generated at one–loop level. As before, neither of these choices is protected by a symmetry, i.e. they are not technically natural. We therefore again expect that  $\mathcal{O}_1$  will be generated by radiative corrections. On the other hand,  $CP$  is violated if for some flavor  $q$ ,

$$\lambda_1 h_2^q \neq 0 \quad \text{or} \quad \lambda_2 h_1^q \neq 0. \quad (2.13)$$

We will discuss both variants of Model II in turn.

### 2.2.1 Model IIa

The matrix element for tree–level DM–quark scattering,  $\chi(p_\chi) + q(p_q) \rightarrow \chi(p'_\chi) + q(p'_q)$ , via  $\phi$  exchange in the  $t$ –channel is given by

$$\mathcal{M}_{\chi q \rightarrow \chi q}^{\text{IIa}} = -\frac{h_2^q}{q^2 - m_\phi^2} \bar{u}(p'_\chi)(\lambda_1 + i\gamma^5 \lambda_2)u(p_\chi) \bar{u}(p'_q)i\gamma^5 u(p_q). \quad (2.14)$$

Taking the vanishing momentum transfer limit,  $q^2 \rightarrow 0$ , in the  $\phi$  propagator, the matrix element can be matched onto the relativistic effective operators  $(\bar{\chi}\chi)(\bar{q}i\gamma^5 q)$  and  $(\bar{\chi}i\gamma^5 \chi)(\bar{q}i\gamma^5 q)$ , which reduce to the operators  $\mathcal{O}_{10}$  and  $\mathcal{O}_6$ , respectively, in the non–relativistic limit. Recall, however, from Table 1 that  $\mathcal{O}_6$  is doubly suppressed by momentum transfer  $\vec{q}$ , therefore generating a cross section suppressed by  $\mathcal{O}(\vec{q}^2/m_N^2) \sim 10^{-2} - 10^{-3}$  relative to the contribution from  $\mathcal{O}_{10}$ . Hence, at the leading order in perturbation theory,  $\mathcal{O}_{10}$  dominates the scattering matrix element in Model IIa.

Although the operator  $\mathcal{O}_1$  is not generated from leading order Feynman diagrams, one–loop corrections to DM–nucleus scattering again include contributions that reduce to  $\mathcal{O}_1$  in the low energy limit; the corresponding Feynman diagrams are shown in Fig. 2.

In this model, there are two different box (and crossed box) diagrams: one involves the scalar coupling  $\lambda_1$  and the other involves the pseudoscalar coupling  $\lambda_2$ . The triangle diagram involves the scalar coupling  $\lambda_1$  between the DM and the mediator,<sup>7</sup> as well as the cubic self–interaction of the mediator  $\mu_1$ . All diagrams contain two vertices with the pseudoscalar coupling  $h_2^q$  on the quark line.

---

<sup>7</sup>There is also a triangle diagram involving  $\lambda_2$ , as well as (crossed) box diagrams with one  $\lambda_1$  vertex and one  $\lambda_2$  vertex; however, these diagrams do not contribute to  $\mathcal{O}_1$ . Moreover, the diagrams shown in Fig. 2 also generate other operators in the non–relativistic limit. We ignore these contributions, since they are of higher order in both the loop and NREFT expansions.

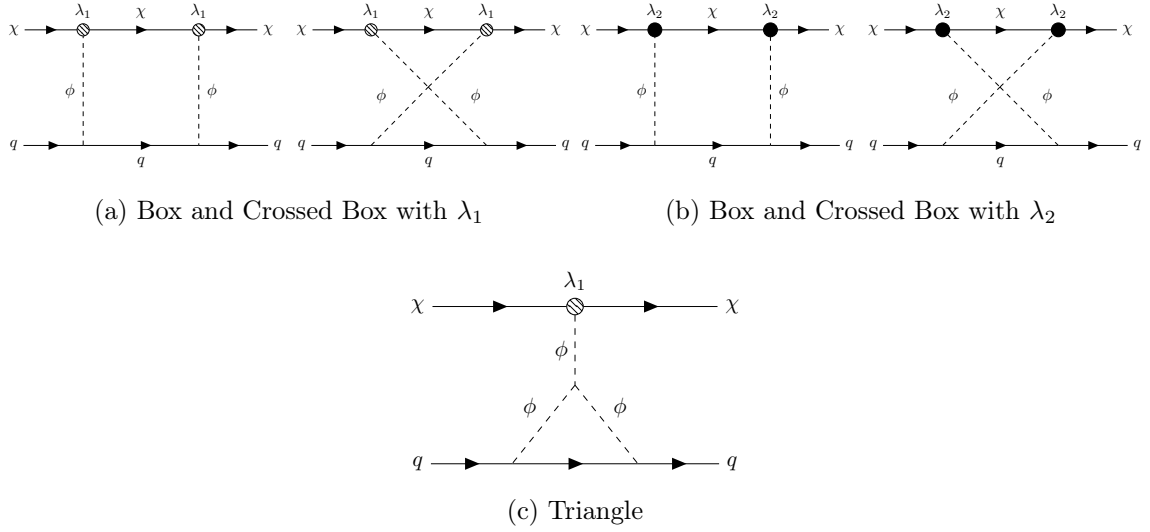


**Figure 2:** One-loop box and triangle Feynman diagrams in Model IIa which contribute to  $\mathcal{O}_1$ . The shaded blob denotes the scalar DM–mediator coupling  $\lambda_1$  while the dark blob denotes the pseudoscalar DM–mediator coupling  $\lambda_2$ .

In order to simplify the loop calculation, we have used the Dirac equation as well as 4–momentum conservation, and took the limit of vanishing momentum transfer. Further details can be found in Appendix A.2. Finally, we find the following effective Lagrangian for Model IIa:

$$\mathcal{L}_{\text{eff}}^{\text{IIa}} \supset c_{10}^{q,d6} (\bar{\chi}\chi) (\bar{q}i\gamma^5 q) + c_6^{q,d6} (\bar{\chi}i\gamma^5\chi) (\bar{q}i\gamma^5 q) + c_{1,S}^{q,d6} (\bar{\chi}\chi) (\bar{q}q) + c_{1,V}^{q,d6} (\bar{\chi}\gamma_\mu\chi) (\bar{q}\gamma^\mu q) ; \quad (2.15)$$

the notation is as in (2.5). For completeness we have retained  $(\bar{\chi}i\gamma^5\chi) (\bar{q}i\gamma^5 q)$  in the set of effective operators, although it can safely be neglected as reasoned earlier. Table 3 displays the list of relativistic effective operators and their matching to the NREFT operators in terms of the parameters of Model IIa. The quark–level Wilson coefficients contain loop-level Wilson coefficients  $N_k(r, s)$ ,  $k = 1, \dots, 8$ ,  $P_l(r, s)$ ,  $l = 1, \dots, 4$  and  $R_1(r)$ , which have been expressed as functions of dimensionless parameters  $r \equiv m_q/m_\phi$  and  $s \equiv m_\chi/m_\phi$ . Analytic expressions for these loop functions can be found in Appendix A.2.1.

Collecting the results of Table 3, and embedding the quark bilinears in nucleonic matrix

	$\bar{\chi}\Gamma_\chi\chi\bar{q}\Gamma_qq$	$c_i^q$
Tree	$c_{10}^{q,d6}\bar{\chi}\chi\bar{q}i\gamma^5q \longrightarrow$	$\frac{h_2^q\lambda_1}{m_\phi^2}$
Box $ \lambda_1$	$c_{1,V,B1}^{q,d6}\bar{\chi}\gamma_\mu\chi\bar{q}\gamma^\mu q \longrightarrow$	$-\frac{\lambda_1^2(h_2^q)^2}{16\pi^2}N_1$
	$c_{1,S,B1}^{q,d6}\bar{\chi}\chi\bar{q}q \longrightarrow$	$-\frac{\lambda_1^2(h_2^q)^2}{16\pi^2}(2m_\chi m_q(N_2 - P_2) + m_\chi^2(N_3 - 2P_1) + m_q^2 N_4)$
Crossed	$c_{1,V,C1}^{q,d6}\bar{\chi}\gamma_\mu\chi\bar{q}\gamma^\mu q \longrightarrow$	$\frac{\lambda_1^2(h_2^q)^2}{16\pi^2}N_5$
Box $ \lambda_1$	$c_{1,S,C1}^{q,d6}\bar{\chi}\chi\bar{q}q \longrightarrow$	$\frac{\lambda_1^2(h_2^q)^2}{16\pi^2}(2m_\chi m_q(N_6 - P_4) + m_\chi^2(N_7 - 2P_3) + m_q^2 N_8)$
Box $ \lambda_2$	$c_{1,V,B2}^{q,d6}\bar{\chi}\gamma_\mu\chi\bar{q}\gamma^\mu q \longrightarrow$	$-\frac{\lambda_2^2(h_2^q)^2}{16\pi^2}N_1$
	$c_{1,S,B2}^{q,d6}\bar{\chi}\chi\bar{q}q \longrightarrow$	$-\frac{\lambda_2^2(h_2^q)^2}{16\pi^2}(2m_\chi m_q N_2 + m_\chi^2 N_3 + m_q^2 N_4)$
Crossed	$c_{1,V,C2}^{q,d6}\bar{\chi}\gamma_\mu\chi\bar{q}\gamma^\mu q \longrightarrow$	$\frac{\lambda_2^2(h_2^q)^2}{16\pi^2}N_5$
Box $ \lambda_2$	$c_{1,S,C2}^{q,d6}\bar{\chi}\chi\bar{q}q \longrightarrow$	$\frac{\lambda_2^2(h_2^q)^2}{16\pi^2}(2m_\chi m_q N_6 + m_\chi^2 N_7 + m_q^2 N_8)$
Triangle	$c_{1,S,T}^{q,d6}\bar{\chi}\chi\bar{q}q \longrightarrow$	$-\frac{\lambda_1\mu_1(h_2^q)^2}{16\pi^2}\frac{m_q}{m_\phi}R_1$

**Table 3:** Non-relativistic reduction of effective operators in Model IIa. In the expression for the quark-level Wilson coefficients, we have again suppressed the dependence of the loop functions on dimensionless parameters, i.e.  $N_k \equiv N_k(r, s)$ ,  $P_l \equiv P_l(r, s)$  and  $R_1 \equiv R_1(r)$ , where  $r \equiv m_q/m_\phi$  and  $s \equiv m_\chi/m_\phi$ . The first line contributes to the coefficient of  $\mathcal{O}_{10}$ , all other lines describe contributions  $\propto \mathcal{O}_1$ .

elements, the Wilson coefficient  $c_1^N$  of the NREFT operator  $\mathcal{O}_1$  is given by

$$\begin{aligned}
c_1^N|_{\text{IIa}} = & -\frac{1}{16\pi^2} \left[ (\lambda_1^2 + \lambda_2^2) \left( \sum_{q=u,d} (h_2^q)^2 \mathcal{N}_q^N (N_1(r, s) - N_5(r, s)) \right) \right. \\
& + m_N \left( \sum_{q=u,d,s} (h_2^q)^2 f_{Tq}^N + \frac{2}{27} f_{TG}^N \sum_{q=c,b,t} (h_2^q)^2 \right) \\
& \times \left\{ (\lambda_1^2 + \lambda_2^2) \left( 2m_\chi (N_2(r_q, s) - N_6(r_q, s)) + \frac{m_\chi^2}{m_q} (N_3(r_q, s) - N_7(r_q, s)) \right) \right. \\
& + m_q (N_4(r_q, s) - N_8(r_q, s)) \\
& - 2m_\chi \lambda_1^2 \left( P_2(r_q, s) - P_4(r_q, s) + \frac{m_\chi}{m_q} (P_1(r_q, s) - P_3(r_q, s)) \right) \\
& \left. \left. + \frac{\lambda_1\mu_1}{m_\phi} R_1(r_q) \right\} \right]. \tag{2.16}
\end{aligned}$$

The nuclear bilinear coefficients  $\mathcal{N}_q^N$ ,  $f_{Nq}^T$  and  $f_{NG}^T$  are the same as in eq.(2.6). At first sight  $c_1^N|^{IIa}$  appears to be singular in the limit  $m_q \rightarrow 0$ . Note that  $f_{Nq}^T$  contains a factor of  $m_q$ , see eq.(2.7); hence contributions to  $c_{1,S}^{q,d6}$  in Table 3 without an explicit factor  $m_q$  appear  $\propto 1/m_q$  in eq.(2.16). However, they get multiplied with the differences of loop functions  $N_3(r_q, s) - N_7(r_q, s)$  or  $P_1(r_q, s) - P_3(r_q, s)$ , which scale like  $r_q$  for  $r_q \rightarrow 0$ ; these contributions therefore approach a finite value as  $m_q \rightarrow 0$ . In contrast, the difference  $N_1(r_q, s) - N_5(r_q, s)$ , which appears in the contribution from the product of two vector currents, vanishes for  $r_q \rightarrow 0$ . As a result, the dominant contributions to  $c_1^N|^{IIa}$  also originate from the product of two scalar currents, as for Model I. Within this category, the contribution  $\propto N_4 - N_8$  vanishes as  $r_q \rightarrow 0$  and is therefore negligible for generation-independent couplings  $h_2^q$ , but all other terms are very roughly comparable and must be taken into account.

The Wilson coefficient of the operator  $\mathcal{O}_{10}$  arising from the  $t$ -channel tree-level scattering diagram is

$$c_{10}^N|^{IIa} = \frac{\lambda_1}{m_\phi^2} \left( \sum_{q=u,d,s} h_2^q \Delta \tilde{q}^N - \Delta \tilde{G}^N \sum_{q=c,b,t} \frac{h_2^q}{m_q} \right). \quad (2.17)$$

## 2.2.2 Model IIb

We next turn to Model IIb. It is also described by the Lagrangian of eq.(2.11), but we now postulate purely scalar Yukawa couplings  $h_1^q$  on the quark side and a purely pseudoscalar coupling  $\lambda_2$  on the dark matter side, see eq.(2.12). The tree-level matrix element for DM-quark scattering,  $\chi(p_\chi) + q(p_q) \rightarrow \chi(p'_\chi) + q(p'_q)$ , proceeding via  $t$ -channel  $\phi$  exchange is then:

$$\mathcal{M}_{\chi q \rightarrow \chi q}^{IIb} = -\frac{h_1^q \lambda_2}{q^2 - m_\phi^2} \bar{u}(p'_\chi) i\gamma^5 u(p_\chi) \bar{u}(p'_q) u(p_q). \quad (2.18)$$

This matrix element matches onto the dimension-6 effective operator  $(\bar{\chi} i\gamma^5 \chi)(\bar{q}q)$ , which reduces to the momentum-suppressed SI NREFT operator  $\mathcal{O}_{11}$  in the non-relativistic limit. Once again, the choice  $\lambda_1 = 0$ , which ensures the absence of  $\mathcal{O}_1$  at tree-level, is not protected by any symmetry. We therefore again expect contributions  $\propto \mathcal{O}_1$  to be generated at the next order in perturbation theory. The relevant Feynman diagrams are shown in Fig. 3. Each diagram involves two factors of the pseudoscalar DM-mediator coupling  $\lambda_2$ ; the two  $\gamma_5$  factors multiply to unity. The triangle and (crossed) box diagrams in addition involve one or two factors of the scalar DM-quark coupling  $h_1^q$ , respectively; the former also involves the cubic self-coupling  $\mu_1$  of the mediator. The triangle diagram can be interpreted as generating a scalar DM-mediator coupling. Explicit expressions for the resulting amplitudes are provided in Appendix A.2.

When the mediator  $\phi$  is integrated out, the following relativistic effective Lagrangian describes DM-quark scattering:

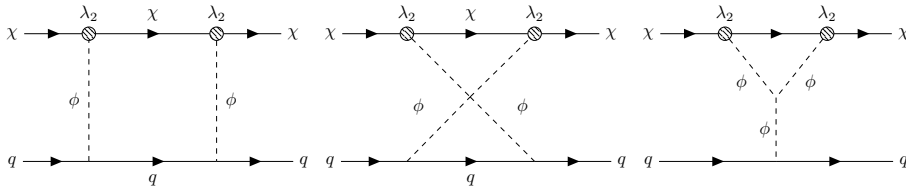
$$\mathcal{L}_{\text{eff}}^{IIb} \supset c_{11}^{q,d6} (\bar{\chi} i\gamma^5 \chi)(\bar{q}q) + c_{1,S}^{q,d6} (\bar{\chi}\chi)(\bar{q}q) + c_{1,V}^{q,d6} (\bar{\chi}\gamma_\mu \chi)(\bar{q}\gamma^\mu q). \quad (2.19)$$

Table 4 displays the quark-level Wilson coefficients in terms of the parameters of Model IIb. The loop functions  $N_k$  and  $P_l$  are identical to the ones appearing in Model IIa.  $S_1$  is

	$\bar{\chi}\Gamma\chi\bar{N}\Gamma_N N$	$c_i^q$
Tree	$c_{11}^{q,d6}\bar{\chi}i\gamma^5\chi\bar{q}\gamma^\mu q \longrightarrow$	$\frac{h_1^q\lambda_2 m_N}{m_\phi^2 m_\chi}$
Box	$c_{1,V,B}^{q,d6}\bar{\chi}\gamma_\mu\chi\bar{q}\gamma^\mu q \longrightarrow$	$-\frac{\lambda_2^2 h_1^{q^2}}{16\pi^2} N_1$
	$c_{1,S,B}^{q,d6}\bar{\chi}\chi\bar{q}q \longrightarrow$	$-\frac{\lambda_2^2 h_1^{q^2}}{16\pi^2} (2m_\chi m_q(N_2 + P_1) + m_\chi^2 N_3 + m_q^2(N_4 + 2P_2))$
Crossed	$c_{1,V,C}^{q,d6}\bar{\chi}\gamma_\mu\chi\bar{q}\gamma^\mu q \longrightarrow$	$\frac{\lambda_2^2 h_1^{q^2}}{16\pi^2} N_5$
Box	$c_{1,S,C}^{q,d6}\bar{\chi}\chi\bar{q}q \longrightarrow$	$\frac{\lambda_2^2 h_1^{q^2}}{16\pi^2} (2m_\chi m_q(N_6 - P_3) + m_\chi^2 N_7 + m_q^2(N_8 - 2P_4))$
Triangle	$c_{1,S,T}^{q,d6}\bar{\chi}\chi\bar{q}q \longrightarrow$	$-\frac{h_1^q \mu_1 \lambda_2^2}{16\pi^2} \frac{m_\chi}{m_\phi} S_1$

**Table 4:** Non-relativistic reduction of effective operators in Model IIb. The arguments of the loop functions  $N_k$ ,  $P_l$  and  $S_1$  have again been suppressed; explicit expressions for these functions can be found in Appendix A.2.1.

the only loop function not defined previously, and its analytic expression along with that of the others can be found in Appendix A.2.1.



**Figure 3:** One-loop (crossed) box and triangle Feynman diagrams in Model IIb which contribute to  $\mathcal{O}_1$  in the non-relativistic limit.

Collecting the results of Table 4, and inserting the appropriate hadronic coefficients for the nucleonic matrix elements of the quark bilinears, the Wilson coefficient of the operator  $\mathcal{O}_1$



is:

$$\begin{aligned}
c_{11}^N|_{\text{Ib}} = & -\frac{\lambda_2^2}{16\pi^2} \left\{ \sum_{q=u,d} \mathcal{N}_q^N (h_1^q)^2 \left( N_1(r_q, s) - N_5(r_q, s) \right) \right. \\
& + m_N \left( \sum_{q=u,d,s} f_{Tq}^N + \frac{2}{27} f_{TG}^N \sum_{q=c,b,t} \right) \\
& \times \left[ (h_1^q)^2 \left( 2m_\chi \left( N_2(r_q, s) - N_6(r_q, s) + P_1(r_q, s) + P_3(r_q, s) \right) \right. \right. \\
& \quad + m_q \left( N_4(r_q, s) - N_8(r_q, s) + 2 \left( P_2(r_q, s) + P_4(r_q, s) \right) \right) \\
& \quad \left. \left. + \frac{m_\chi^2}{m_q} \left( N_3(r_q, s) - N_7(r_q, s) \right) \right) \right] \\
& \left. + \mu_1 h_1^q \frac{m_\chi}{m_\phi} \frac{S_1(s)}{m_q} \right\}; \tag{2.20}
\end{aligned}$$

recall that  $r_q = m_q/m_\phi$  and  $s = m_\chi/m_\phi$ . As in case of Model IIa, the combinations of loop functions multiplying  $\mathcal{N}_q^N$  and  $m_\chi^2/m_q$  vanish for  $m_q \rightarrow 0$ ; the term  $\propto m_\chi^2/m_q$  thus yields a finite result in this limit. However, the very last term in eq.(2.20) also contains an explicit  $1/m_q$  factor; the loop function appearing in this term does not depend on  $m_q$  at all. Here the required chirality breaking on the quark line is due to the *single* factor of  $h_1^q$ . We therefore expect this term to dominate, unless the trilinear scalar coupling  $\mu_1$  is for some reason very small.

From eq.(2.18) the tree-level contribution to the Wilson coefficient of  $\mathcal{O}_{11}$  is:

$$c_{11}^N|_{\text{Ib}} = \frac{\lambda_2}{m_\phi^2} \frac{m_N^2}{m_\chi} \left( \sum_{q=u,d,s} \frac{h_1^q f_{Tq}^N}{m_q} + \frac{2}{27} f_{TG}^N \sum_{q=c,b,t} \frac{h_1^q}{m_q} \right) = \frac{\lambda_2}{m_\phi^2} \frac{m_N^2}{m_\chi} \tilde{f}^N. \tag{2.21}$$

Here we have defined  $\tilde{f}^N \equiv \left( \sum_{q=u,d,s} \frac{h_1^q f_{Tq}^N}{m_q} + \frac{2}{27} f_{TG}^N \sum_{q=c,b,t} \frac{h_1^q}{m_q} \right)$ , and as usual neglected the  $q^2$  term in the  $\phi$  propagator. As in the last term in eq.(2.20) the required chirality breaking on the quark line is provided by  $h_1^q$ . Since the hadronic matrix elements  $f_{Tq}^N$  have been defined including an explicit factor of  $m_q$ , the contributions in  $\tilde{f}^N$  scale  $\propto 1/m_q$ , leading to a large enhancement of the contribution of light quarks. On the other hand, an extra factor  $m_N/m_\chi$  appears since the pseudoscalar DM current is  $\propto |\vec{q}|/m_\chi = (|\vec{q}|/m_N) \times (m_N/m_\chi)$ . As already noted in the discussion of Table 1, this appears to be quite generic [47–50].

### 2.3 The Neutron EDM

In all three cases we considered, the tree-level contribution to the Wilson coefficient of  $\mathcal{O}_{10}$  or  $\mathcal{O}_{11}$  is nonzero only if  $CP$  is violated: in Model I one needs  $g_1 h_2^q \neq 0$ , where  $g_1$  is a scalar coupling while  $h_2^q$  is a pseudoscalar coupling; in Model IIa,  $\lambda_1 h_2^q \neq 0$  is required, where  $\lambda_1$  is a scalar coupling; and in Model IIb,  $c_{11}^{d6} \propto \lambda_2 h_1^q$ , where  $\lambda_2$  is pseudoscalar but  $h_1^q$  is scalar. Since we assume the quark Yukawa couplings to be flavor diagonal, the most sensitive probe

of  $CP$  violation is the EDM of the neutron (or of heavier nuclei). However,  $CP$  violation is a necessary condition for the generation of an EDM; it is not by itself sufficient. In the case at hand, since we set  $h_1^q = 0$  in Models I and IIa and  $h_2^q = 0$  in Model IIb, there is no one-loop contribution to the neutron EDM, in contrast to the models with charged mediator we considered in ref.[50]. In case of Model IIb, as far as the one-loop diagram with a quark and a mediator  $\phi$  in the loop is concerned, the mediator can consistently be defined as being  $CP$ -even, since only the coupling  $h_1^q$  appears in the diagram. Similarly, in Model I and Model IIa, in the one-loop diagram with a quark-mediator loop the mediator can consistently be defined as being  $CP$ -odd, since only the coupling  $h_2^q$  appears.

Turning to higher loops, a  $CP$ -even mediator can have any self coupling. Hence in Model IIb embellishing the one-loop diagram with additional scalar vertices does not lead to  $CP$  violation. In fact, in this model the only coupling that is not consistent with interpreting  $\phi$  to be  $CP$ -even is  $\lambda_2$ , which couples  $\phi$  to the DM particle. However, this coupling cannot contribute to electric dipole moments. It could appear in any diagram where the only external particles are a through-going quark and a photon (or gluon) only via a closed  $\chi$  loop, which will either vanish (if an odd number of  $\phi$  legs is attached to it), or simply renormalize a  $CP$ -even quantity like the  $\phi$  2-point function. We thus conclude that in Model IIb, *no* new contributions to the electric dipole moments of SM particles are generated. The conceptually easiest way to prove the existence of  $CP$  violation in this model is via  $\chi q$  scattering; in case of  $2 \rightarrow 2$  scattering, spin observables would have to be included in the construction of a  $CP$ -odd quantity. While conceptually straightforward, experimentally this seems prohibitively difficult; certainly there are no current experimental constraints from such experiments.

The situation is very different in Models I and IIa, where in the relevant one-loop diagram the mediator behaves like a pseudoscalar. The reason is that a pseudoscalar cannot have a  $\phi^3$  coupling. Hence, two-loop diagrams containing both the (pseudoscalar) Yukawa coupling  $h_2^q$  and the (scalar) trilinear coupling  $\mu_1$ , see Fig. 4, can be expected to generate a nonvanishing (chromo-)EDM for quark  $q$ . It should be noted that here  $\mu_1$  is relevant, not the couplings  $\lambda_1$  or  $g_1$  appearing in the coefficient of  $\mathcal{O}_{10}$ . However, a theory with  $\mu_1 = 0$  but  $\lambda_1 \neq 0$  is, strictly speaking, not renormalizable, since a triangle diagram with  $\chi$  in the loop will generate a *divergent* contribution to  $\mu_1 m_\phi \propto m_\chi \lambda_1^3$ ; similarly, in Model I there are divergent one-loop contributions  $\propto g_1 g_2 m_S$  to the  $\phi^3$  vertex. We will come back to this point later. Because only the trilinear self-coupling of the mediator and its pseudoscalar Yukawa coupling to quarks are relevant here, the calculation of the quark (chromo) EDM is exactly the same in these two models.

The quark EDM  $d_q$  is calculated as the coefficient of a dimension-5  $P$ - and  $T$ -odd interaction term  $(-i/2) \bar{q} \sigma_{\mu\nu} \gamma_5 q F^{\mu\nu}$  at zero momentum transfer. The same quark radiating a gluon instead a photon leads to non-vanishing chromo EDM. These are calculated similar to quark EDMs, by finding the coefficient of  $(-i/2) \bar{q} \sigma_{\mu\nu} t_a \gamma_5 q G_a^{\mu\nu}$  at zero momentum transfer.

The EDM operator breaks chirality, hence  $d_q$  is proportional to an odd number of chirality flips. These can come either from fermion masses or from Yukawa couplings in the relevant Feynman diagrams. The diagrams shown in Fig. 4 contain three Yukawa couplings, hence

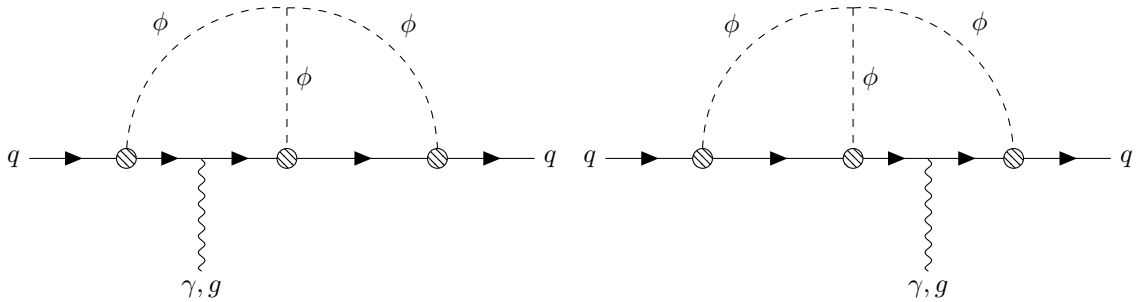


**Figure 4:** Two-loop Feynman diagrams for quark EDMs and color-EDMs in Model I and IIa. The blobs here indicate the insertion of the mediator pseudoscalar Yukawa coupling.

they can contribute even for  $m_q \rightarrow 0$ . We provide the details of the computation of these two-loop diagrams in Appendix B. We calculate the quark EDM to be

$$d_q = \frac{2e Q_q (h_2^q)^3}{(16\pi^2)^2} \mu_1 m_\phi \lim_{q^2 \rightarrow 0} \left( [\mathcal{X}] + [\mathcal{Y}] \right), \quad (2.22)$$

where  $Q_q$  is the electric charge of quark  $q$ ;  $[\mathcal{X}]$  and  $[\mathcal{Y}]$  are loop functions expressed as five dimensional integrals over five Feynman parameters given in eqs.(B.19) and (B.20). The color-EDM  $\tilde{d}_q$  can be obtained by replacing the external photon with a gluon. Hence  $\tilde{d}_q$  can be obtained from eq.(2.22) by replacing  $eQ_q$  with the strong coupling  $g_s$ .

In order to calculate the value of the nEDM from  $d_q$  and  $\tilde{d}_q$ , we use

$$d_n = g_T^u d_u + g_T^d d_d + g_T^s d_s + 1.1 e (0.5 \tilde{d}_u + \tilde{d}_d). \quad (2.23)$$

Here the tensor charges  $g_T^u = -0.233(28)$ ,  $g_T^d = 0.774(66)$  and  $g_T^s = 0.009(8)$  have been calculated using lattice QCD [59, 60] (see also Refs.[61–63]) at a renormalization scale of 2 GeV. We are not aware of a reliable lattice computation of the contribution of the chromo-EDMs to  $d_n$ ; we therefore employ a computation using QCD sum rules, again evaluated at a renormalization scale of 2 GeV [64], although there is an  $\mathcal{O}(50\%)$  uncertainty in these results [65, 66]. In this case the uncertainty in the coefficients in Eq.(2.23) might shift the boundary of the excluded region slightly, without affecting our results qualitatively. Since in our numerical analyses we will assume flavor universal quark Yukawa couplings, the contributions from the (chromo-)EDMs of heavy quarks to the EDM of the neutron can safely be neglected; in fact, since  $g_T^s \ll g_T^d$  already the contribution from the strange quark is essentially negligible for equal couplings.

### 3 Results and Discussions

In the previous section, we described the different contributions to DM–nucleus scattering in Models I, IIa and IIb. These simplified models were designed such there are no tree-level contributions to the NREFT operator  $\mathcal{O}_1$ ; instead, at tree-level only the  $P$ - and  $T$ -odd operators  $\mathcal{O}_{10}$  (in Model I and IIa) or  $\mathcal{O}_{11}$  (in Model IIb) were generated. Recall that  $\mathcal{O}_1$  often gives the dominant contribution to DM–nucleus scattering: it appears in

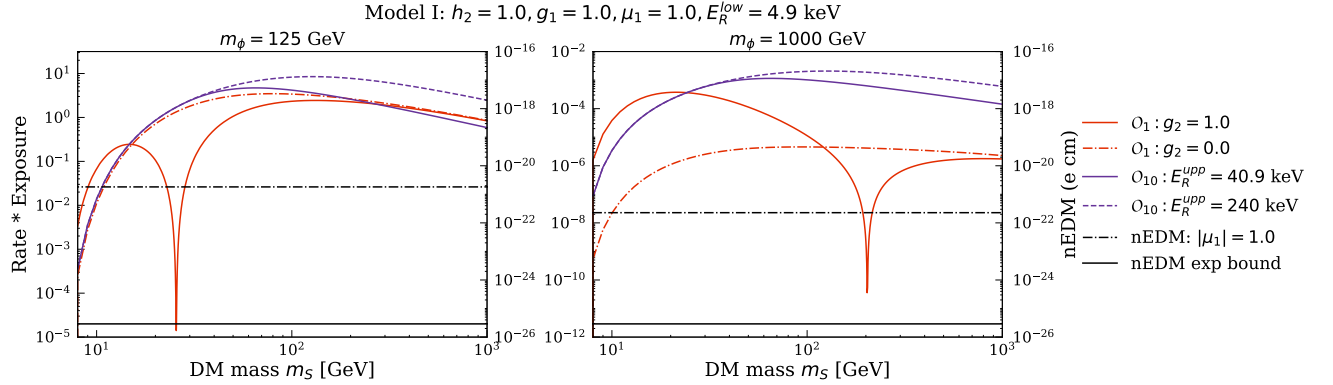


**Figure 5:** The left  $y$ -axis shows the total number of scattering events in Model I with  $\mu_1 = 1.0$  at XENON1T with a run time exposure of 1 tonne-year as a function of the DM mass  $m_S$  for two values of the mediator mass,  $m_\phi = 125 \text{ GeV}$  (left frame) and  $m_\phi = 1000 \text{ GeV}$  (right frame). The **violet** and **red** curves show the number of events due to  $\mathcal{O}_{10}$  and  $\mathcal{O}_1$ , respectively. The **black** lines refer to the right  $y$ -axis; the **solid black** line is the experimental upper limit on nEDM at 90% C.L., while the **dashed black** line is the predicted nEDM for the given choice of parameters.

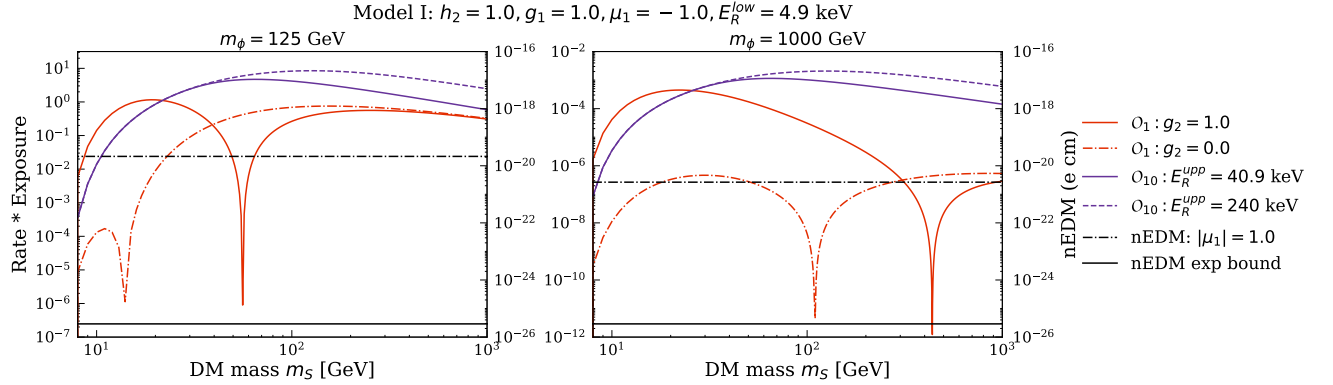
leading order in the NREFT expansion, and its contribution is coherently enhanced by  $A^2$  if  $c_1^n \simeq c_1^p$ , where  $c_1^n$  and  $c_1^p$  are the Wilson coefficients accompanying  $\mathcal{O}_1$  for neutron and proton respectively. However, in the models considered here,  $\mathcal{O}_1$  arises from box and triangle diagrams appearing at next-to-leading order in perturbation theory. Therefore, it is not obvious *a priori* which operator provides the dominant contribution to DM-nucleus scattering.

In this section we compare the contributions from  $\mathcal{O}_1$  quantitatively to the contributions from  $\mathcal{O}_{10}$  or  $\mathcal{O}_{11}$ . To that end, we compute the number of events due to these operators for a recent XENON1T run [2] for a variety of benchmark model parameters. Here we use the explicit expressions for the loop functions contributing to the Wilson coefficient of  $\mathcal{O}_1$  given in Appendix A. It should be noted that the contribution from  $\mathcal{O}_1$  does not interfere with those from  $\mathcal{O}_{10}$  and  $\mathcal{O}_{11}$ , due to the different  $CP$  properties of these operators. Hence the total scattering rate is simply given by the sum of these contributions.<sup>8</sup>

Moreover, for Models I and IIa we check numerically if the nEDM surpasses its experimental upper bound [44–46]. We perform the integration of the loop functions in eq.(2.22) using the Monte Carlo integration routine **SUAVE** of the **CUBA** numerical library [67]. The absolute numerical error reported by the routine is around  $\mathcal{O}(10^{-8})$  for the two values of the mediator mass  $m_\phi$  we consider.

In order to compute the number of events for the 2018 run of XENON1T [2], we integrate the differential event rate, computed using the the Mathematica code **dmformfactor**, which is based on the formalism of ref.[20], over the recoil energy  $E_R$  from 4.9 keV to 40.9 keV,

<sup>8</sup>Recall that we only extract the contribution to  $\mathcal{O}_1$  from our loop diagrams. These diagrams will also contribute to additional NREFT operators; however, those contributions will be of higher order both in the loop and NREFT expansions, and can thus safely be neglected.



in accordance with the recoil energy region of interest (ROI) used in that run. In addition, we include results (shown as dashed curves) where the upper end of integration is set at  $E_R^{upp} = 240 \text{ keV}$ , as considered in a dedicated effective field theory search by the XENON experiment. We multiply the integrated rate with the 2018 XENON1T runtime exposure of  $278.8 \text{ days} \times 1.3 \text{ tonne} = 1.0 \text{ tonne}\cdot\text{yr}$ . We have further assumed a standard isothermal DM halo with  $\rho_\chi = 0.3 \text{ GeVcm}^{-3}$ ,  $v_0 = 220 \text{ km/s}$ ,  $v_e = 232 \text{ km/s}$  and  $v_{esc} = 544 \text{ km/s}$ . We calculate our event rates using a weighted sum over the different isotopes occurring in naturally abundant Xenon.

We choose the following sets of parameter values for Model I:  $h_2^q \equiv h_2 = g_1 = 1.0$  with  $m_\phi = 125 \text{ GeV}$  or  $m_\phi = 1000 \text{ GeV}$ . Note that we choose a rather large and flavor universal Yukawa coupling of the quarks. For the given couplings, the former (smaller) mediator mass value leads to a DM–nucleon cross section from the operator  $\mathcal{O}_{10}$  that lies just below the sensitivity of the 2018 XENON1T run in the  $\sigma_{\chi p} - m_S$  exclusion plane. The latter (larger) mediator mass corresponds to a DM–nucleon cross section from the operator  $\mathcal{O}_{10}$  that lies just above the irreducible background from coherent neutrino–nucleus scattering (the so–called “neutrino floor”); it will be very difficult to probe even smaller cross sections in direct search experiments.

Figures 5 and 6 depict the resulting number of events from the operators  $\mathcal{O}_{10}$  and  $\mathcal{O}_1$  as a function of the DM mass  $m_S$  in Model I, for different values of the trilinear mediator coupling  $\mu_1$ . Each figure contains two frames, corresponding to the two values of  $m_\phi$  we consider.

Since the tree–level contribution from  $\mathcal{O}_{10}$  does not depend on  $\mu_1$ , it remains the same in both figures. We note that this contribution is enhanced by up to an order of magnitude once the DM mass  $m_S$  exceeds the mass of the target nuclei ( $\simeq 125 \text{ GeV}$  for Xenon) if the upper end of the ROI is increased from  $40.9 \text{ keV}$  to  $240 \text{ keV}$ . This is not surprising, since  $\mathcal{O}_{10}$  predicts a recoil energy spectrum that peaks at sizable energy, due to the explicit factor of  $\vec{q}$  that appears in the definition of this operator. Note that at  $m_S < m_{Xe}$ , the maximal recoil energy is  $\mathcal{O}(v^2 m_S^2 / m_{Xe})$  rather than  $\mathcal{O}(v^2 m_{Xe})$  for  $m_S > m_{Xe}$ ; hence this enhancement only occurs at larger DM masses.

Figure 5 is for  $\mu_1 = 1.0$ . We see that the contribution from  $\mathcal{O}_{10}$  generally exceeds that

from  $\mathcal{O}_1$ , except at low DM mass where the low maximal recoil energy leads to low values of  $|\vec{q}|$ . We also note that for  $g_2 = 0$ , i.e. in the absence of the last diagram in Fig. 1, the  $\mathcal{O}_1$  contribution, shown by the dashed red lines, drops faster with increasing  $m_\phi$  than the (tree-level) contribution from  $\mathcal{O}_{10}$  does. For a positive coupling  $g_2 = 1.0$  the contributions from the (crossed) box and  $g_2$  triangle diagrams have opposite signs, leading to a vanishing  $\mathcal{O}_1$  contribution for  $m_S \simeq 0.2m_\phi$ .

In order to understand the comparison of the tree-level  $\mathcal{O}_{10}$  contributions with the loop suppressed  $\mathcal{O}_1$  contributions semi-quantitatively, we estimate the ratio of the number of events from the two contributions  $N_{\mathcal{O}_1}/N_{\mathcal{O}_{10}}$  as:

$$\frac{N_{\mathcal{O}_1}}{N_{\mathcal{O}_{10}}}\Big|_{\text{I}} = \frac{R_{\mathcal{O}_1}}{R_{\mathcal{O}_{10}}}\Big|_{\text{I}} \sim \frac{(c_1^N|_{\text{I}})^2}{(c_{10}^N|_{\text{I}})^2} \frac{A^2}{\langle S_{\text{Xe}} \rangle^2} \frac{m_N^2}{\vec{q}^2}. \quad (3.1)$$

Here  $R_{\mathcal{O}_i}$  denotes the scattering rate due to operator  $\mathcal{O}_i$  integrated over the recoil energy window. The factor  $(\vec{q}^2/m_N^2)^{-1}$  is due to the momentum suppression of  $\mathcal{O}_{10}$ . In this estimate, we have assumed the nuclear response functions to be independent of the recoil energy, and approximated the ratio of the nuclear response functions as  $A^2/\langle S_N \rangle^2$  since the SI response (from  $\mathcal{O}_1$ ) is coherently enhanced by  $A^2$  while the SD response (from  $\mathcal{O}_{10}$ ) is suppressed by the spin expectation value squared  $\langle S_{\text{Xe}} \rangle^2$ . We estimate  $c_1^N|_{\text{I}}$  using the vanishing quark mass limit of eq.(2.6):

$$c_1^N|_{m_q \rightarrow 0}^{\text{I}} = \frac{h_2^2}{16\pi^2} m_N f_T^N \left\{ g_1^2 m_S (M_2 + M_4)|_{r \rightarrow 0} + \left( \frac{g_1 \mu_1}{m_\phi} - \frac{g_2}{2m_S} \right) L_1(r)|_{r \rightarrow 0} \right\}. \quad (3.2)$$

For small  $s = m_S/m_\phi$  and  $g_2 = 1.0$ , the last (triangle) term in eq.(3.2) dominates:

$$c_1^N|_{\text{I}} \approx \frac{h_2^2}{16\pi^2} \frac{g_2}{4} m_N f_T^N \frac{1}{m_S} \frac{1}{m_\phi^2}, \quad (3.3)$$

where we used  $L_1(0) = -1/2m_\phi^2$  and defined  $f^N \equiv \left( \sum_{u,d,s} f_{Tq}^N + \frac{2}{27} f_{TG}^N \sum_{c,b,t} \right)$ . Inserting eq.(3.3) and eq.(2.9) for  $c_{10}^N|_{\text{I}}$  in eq. (3.1), we obtain for  $m_S < m_\phi = 1000$  GeV:

$$\frac{N_{\mathcal{O}_1}}{N_{\mathcal{O}_{10}}}\Big|_{\text{I}} \approx \left( \frac{h_2}{16\pi^2} \frac{g_2}{4g_1} \frac{f_T^N}{\tilde{\Delta}^N} \frac{m_N}{m_S} \right)^2 \frac{A}{\langle S_N \rangle^2} \frac{m_N}{2E_R}, \quad (3.4)$$

where we defined  $\tilde{\Delta}^N = \left( \sum_{q=u,d,s} \Delta \tilde{q}^N - \Delta \tilde{G}^N \sum_{q=c,b,t} \frac{1}{m_q} \right)$  and used  $m_{\text{Xe}} = Am_N$ . Plugging in  $h_2 = g_1 = g_2 = 1.0$ ,  $E_R = 30$  keV for Xenon ( $A = 131$ ) at  $m_S = 30$  GeV results in a ratio of 0.8, which agrees well with the solid red curve for  $\mathcal{O}_1$  being marginally below the purple curve for  $\mathcal{O}_{10}$  in the right frame of Figure 5.

For  $m_\phi = 125$  GeV and not too large  $m_S$   $c_1^N|_{\text{I}}$  is instead dominated by the scattering contribution from the  $g_1$  triangle diagram since  $g_1 \mu_1/m_\phi$  is less suppressed than  $g_2/2m_S$ . In that case we should replace  $g_2/(2m_S)$  by  $g_1 \mu_1/m_\phi$  in eq.(3.4). Again using  $E_R = 30$  keV and  $h_2 = g_1 = \mu_1 = 1.0$ , the estimated contribution from  $\mathcal{O}_1$  is then 0.2 times that from  $\mathcal{O}_{10}$ . This is in good agreement with the left panel of Figure 5 for  $m_S \geq 100$  GeV, above the accidental cancellation around  $m_S \simeq 30$  GeV.

For  $m_S > m_\phi$  and unit couplings, the box diagrams instead dominate, in which case

$$c_1^N|_I \approx \frac{h_2^2 g_1^2}{16\pi^2} f_T^N m_N m_S (M_2 + M_4)|_{r \rightarrow 0} . \quad (3.5)$$

The ratio of the number of scattering events then becomes

$$\frac{N_{\mathcal{O}_1}}{N_{\mathcal{O}_{10}}}|_I \approx \left( \frac{h_2 g_1}{16\pi^2} \frac{f_T^N}{\Delta^N} m_N m_S m_\phi^2 (M_2 + M_4)|_{r \rightarrow 0} \right)^2 \frac{A}{\langle S_N \rangle^2} \frac{m_N}{2E_R} . \quad (3.6)$$

Using  $E_R = 30$  keV and  $h_2 = g_1 = \mu_1 = 1.0$ , for  $m_S = 1000$  GeV and  $m_\phi = 125$  GeV the estimated number of events for  $\mathcal{O}_1$  is 2.8 times that for  $\mathcal{O}_{10}$ . The left panel of Fig. 5 shows that this is a slight overestimate even if the smaller ROI is used. For the larger maximal recoil energy,  $E_R^{\text{upp}} = 240$  keV,  $\mathcal{O}_{10}$  still contributes roughly three times more scattering events than  $\mathcal{O}_1$ . Using the same couplings, for  $m_S = m_\phi = 1000$  GeV, the estimated contribution from  $\mathcal{O}_1$  is smaller by a factor  $2.5 \times 10^{-2}$  relative to that from  $\mathcal{O}_{10}$ . This rough estimate matches the ratio between the  $\mathcal{O}_1$  and  $\mathcal{O}_{10}$  contributions in the right frame of Figure 5.

In Fig. 6 we have changed the sign of  $\mu_1$  while keeping  $g_1$  and  $g_2$  positive (or zero). Both triangle diagrams therefore now contribute with opposite signs than the (crossed) box diagrams. As a result, the coefficient of  $\mathcal{O}_1$  now vanishes at  $m_S \simeq 0.5m_\phi$  for  $g_2 = 1.0$ , and at  $m_S \simeq 0.1m_\phi$  for  $g_2 = 0$ .

As before, for  $g_2 = 1.0$  and small DM masses the Wilson coefficient of  $\mathcal{O}_1$  can be approximated by the triangle diagram involving the  $g_2$  coupling. From eq.(3.4) for  $m_S = 100$  GeV,  $m_\phi = 1000$  GeV and  $h_2 = g_1 = 1.0$  we estimate  $7.2 \times 10^{-2}$  as ratio of the  $\mathcal{O}_1$  and  $\mathcal{O}_{10}$  contributions, in rough agreement with the right panel of Fig. 6. For  $m_S > m_\phi$ , the box diagrams again dominate. Since they do not depend on  $\mu_1$  our earlier estimates still apply. However, since the triangle diagrams aren't quite negligible even at  $m_S = 8m_\phi$ , the largest ratio covered in Fig. 6, this somewhat overestimates the importance of  $\mathcal{O}_1$ .

Before turning to the neutron EDM, we discuss results for DM–Xenon scattering for Model IIa. We again chose a flavor–universal Yukawa coupling  $h_2^q \equiv h_2 = 1$ , and the same two values of mediator mass as for Model I. The coupling  $\lambda_1$  appearing in  $c_{10}$  is set to 1, and we show results for the pseudoscalar mediator–WIMP coupling  $\lambda_2 = 1$  or 0.

Figure 7 shows the number of scattering events from  $\mathcal{O}_{10}$  and  $\mathcal{O}_1$  for  $\mu_1 = 1.0$ . We again find that for the large mediator mass ( $m_\phi = 1000$  GeV, right frame) the tree–level contribution from  $\mathcal{O}_{10}$  dominates by approximately two orders of magnitude for the entire range of  $m_\chi$  shown.<sup>9</sup> On the other hand, for  $m_\phi = 125$  GeV the two contributions are roughly comparable, with  $\mathcal{O}_1$  dominating at small WIMP masses and  $\mathcal{O}_{10}$  dominating for larger masses, in particular if the upper cut on the recoil energy is relaxed to 240 keV.

The main qualitative difference to the results of Model I is that  $c_1$  remains nonzero over the entire range of DM mass shown. The terms from the scalar–scalar current  $\propto \lambda_1^2 + \lambda_2^2$  in eq.(2.16), third line, contribute with opposite sign from those  $\propto \lambda_1^2$  (in the fifth line), which have the same sign as the contribution from the triangle diagram (the last term).

<sup>9</sup>Due to the lower cut on the recoil energy and the upper limit on the WIMP velocity related to the galactic escape velocity, the entire scattering rate vanishes for WIMP masses below 5 GeV.

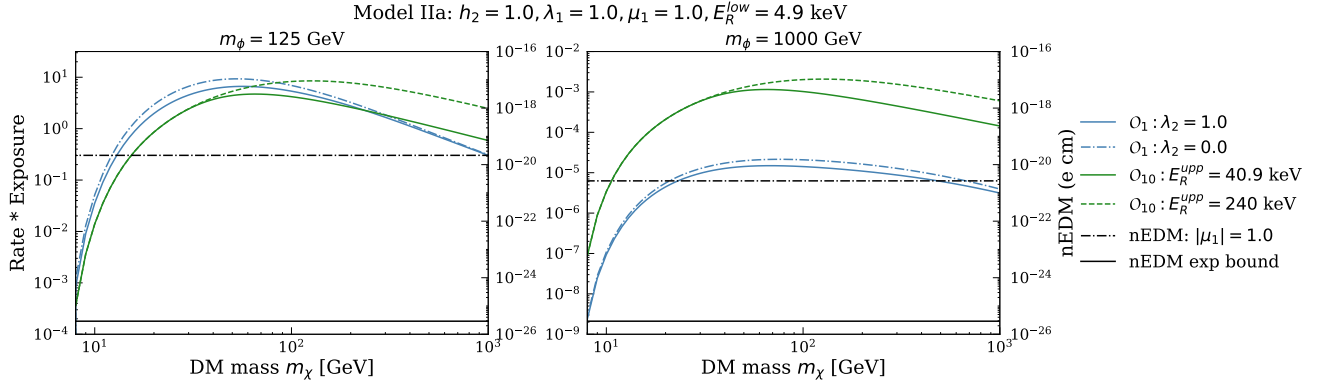


**Figure 7:** The left  $y$ -axes show the total number of scattering events in Model IIa with  $\mu_1 = 1.0$  at XENON1T with a runtime exposure of 1 tonne-year as a function of the DM mass  $m_\chi$  for two values of the mediator mass,  $m_\phi = 125$  GeV (left frame) and  $m_\phi = 1000$  GeV (right frame). The **green** and **blue** curves show the number of events due to  $\mathcal{O}_{10}$  and  $\mathcal{O}_1$  respectively. The **black** lines refer to the right  $y$ -axes; **solid black** line is the experimental upper limit on the nEDM, and the **dashed black** line is value of nEDM predicted by Model IIa.

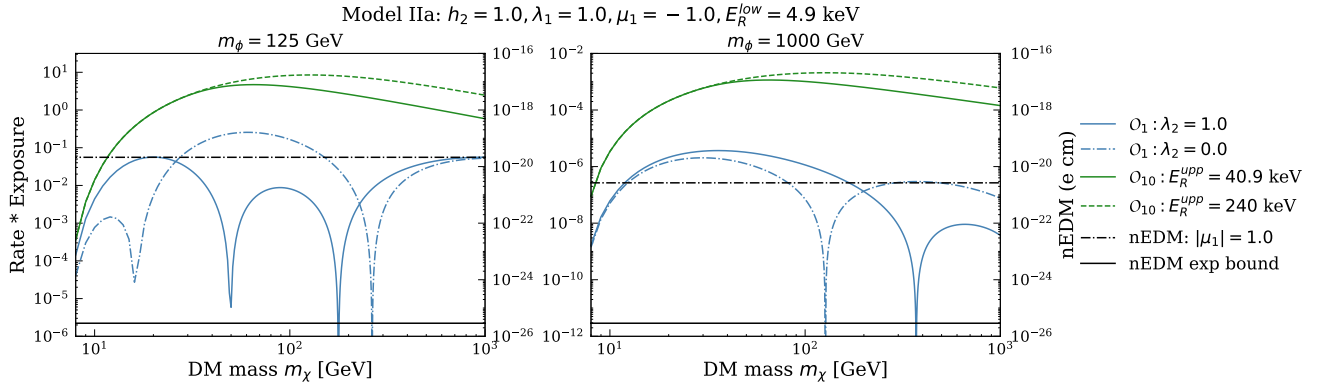


**Figure 8:** As in Fig. 7, but for  $\mu_1 = -1.0$ .

This last (triangle) term dominates both for  $m_\chi \ll m_\phi$  and for  $m_\chi \gg m_\phi$ , but is slightly smaller than the total contribution from box diagrams for  $m_\chi \sim m_\phi$ . As a result, when the (relative) sign between these contributions is flipped by choosing  $\mu_1 = -1$ , as in Fig. 8,  $c_1$  vanishes at the two values of  $s = m_\chi/m_\phi$  where the total box contribution has the same magnitude as the contribution from the triangle diagram. Since this cancellation happens at fixed values of  $s$ , it occurs at larger  $m_\chi$  when  $m_\phi$  is increased (right frame).

The upshot of this discussion is that both in Model I and in Model IIa the contribution from the non-leading NREFT operator  $\mathcal{O}_{10}$  can indeed dominate the loop suppressed contribution from the leading operator  $\mathcal{O}_1$ , especially for large mediator masses. However, we saw at the end of the previous Chapter that in these models an nEDM is produced by two-loop diagrams involving a quark and the mediator  $\phi$ , see Fig. 4. Its 90% C.L. experimental upper



bound is depicted by the solid black curves in Figs 5 to 8 which refer to the right  $y$ -axes, while the nEDM predicted by the models for the given choice of parameters is shown by the dashed black curves. We estimate the numerical value of the nEDM from the dominant contribution from the down quark cEDM  $\tilde{d}_d$ . Using eqs.(2.22) and (2.23), we obtain for  $h_2 = \mu_1 = 1.0$ :

$$|d_n| \approx \frac{2g_S}{(16\pi^2)^2} \left( \frac{m_\phi}{\text{GeV}} \right) \frac{5.28 \times 10^{-2}}{(m_\phi/\text{GeV})^2} e \cdot \text{GeV}^{-1} \approx \frac{1.58 \times 10^{-19}}{(m_\phi/\text{GeV})} e \cdot \text{cm} , \quad (3.7)$$

where we used  $g_S = 1.9$  for the strong coupling at scale of a few GeV. The loop integrals in eq.(2.22) only depend on the quark mass  $m_q$  and the mediator mass  $m_\phi$ . On dimensional grounds, they can be written as  $1/m_\phi^2$  times a function of the dimensionless ratio  $m_q/m_\phi$ . For the down quark we can safely set  $m_q \rightarrow 0$  for the values of  $m_\phi$  we consider; the loop integral then evaluates to  $5.28 \times 10^{-2}/m_\phi^2$ . Eq.(3.7) therefore predicts  $|d_n| \sim \mathcal{O}(10^{-21}) e \cdot \text{cm}$  for  $m_\phi = 125$  GeV. Increasing  $m_\phi$  to 1 TeV reduces the nEDM value by a factor of 8; recall that we parameterize the trilinear scalar coupling as  $\mu_1 m_\phi$ , so for fixed  $|\mu_1|$ ,  $d_n \propto 1/m_\phi$ . This agrees with the dashed black lines in the panels of Figs. 5 to 8.

Evidently for this set of couplings and  $m_\phi = 125$  GeV, the predicted nEDM exceeds the upper bound by about 5 orders of magnitude; increasing  $m_\phi$  to 1 TeV still leads to a discrepancy by about 4 orders of magnitude. Clearly these sets of parameters, which led to in principle observable effects from  $\mathcal{O}_{10}$ , are not realistic.

We saw in eq.(2.22) that the predicted nEDM scales like  $h_2^3 \mu_1$ . In order to suppress the produced nEDM below the upper limit, one thus has to reduce this product of couplings by  $\mathcal{O}(10^{-4} - 10^{-5})$ . This could be achieved by reducing the Yukawa coupling  $h_2$  by a factor of at least 30 while keeping  $|\mu_1| = 1.0$  the same. However, this would reduce the contribution from  $\mathcal{O}_{10}$  to the scattering rate by a factor of  $10^3$ ; the contribution from  $\mathcal{O}_1$  would even be reduced by a factor of  $10^6$ . The resulting cross sections lie below their corresponding neutrino floor(s); this part of parameter space of Models I and IIa is thus beyond the sensitivity of direct search experiments.

Alternatively one can reduce  $\mu_1$  by a factor  $\geq 10^4$ . This effectively removes one of the triangle diagrams contributing to  $\mathcal{O}_1$ , but the contribution from  $\mathcal{O}_{10}$  as well as the box and – for Model I – the second triangle diagram for  $\mathcal{O}_1$  remain unchanged. The contribution from  $\mathcal{O}_{10}$  would then still dominate over that  $\mathcal{O}_1$ , except for small  $m_S$  as discussed above. However, setting  $\mu_1 = 0$  does not increase the symmetry of the theory. Therefore setting  $\mu_1$  to zero only suppresses it at the lowest order in perturbation theory. Radiative corrections will in general induce a non-zero value of this cubic self-coupling.

As shown in Fig. 9, this happens at one-loop level in both Model I and Model IIa, via triangle diagrams with the DM particle running in the loop. Crucially, in both cases the DM-mediator coupling used here is the same coupling that appears in  $c_{10}$ , i.e. one cannot “switch off” these triangle diagrams without simultaneously setting the contribution from  $\mathcal{O}_{10}$  to zero. In case of Model IIa, the diagram shown in Fig. 9 is (logarithmically) divergent, i.e. setting  $\mu_1 = 0$  leads, strictly speaking, to a non-renormalizable theory. The triangle diagram shown for Model I is convergent. If the quartic coupling  $g_2$  is nonzero, there is also

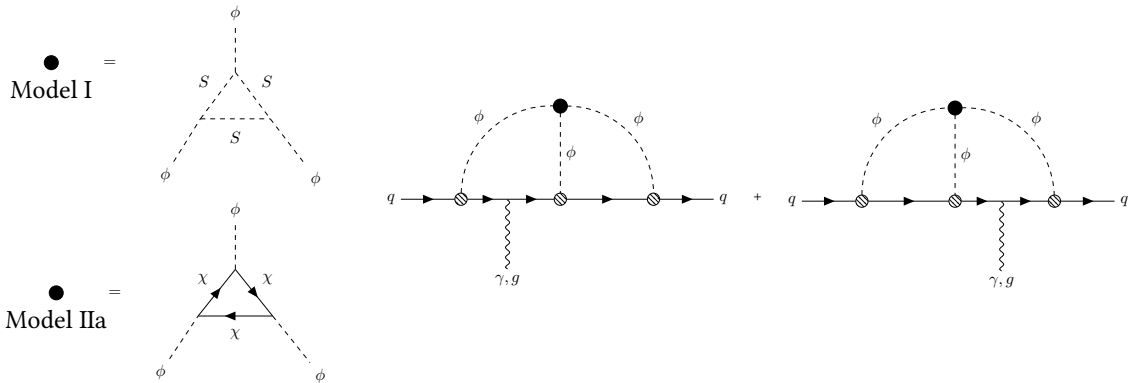


**Figure 9:** One-loop radiative corrections to the three-point function of the mediator  $\langle\phi^3\rangle$  given by triangle diagrams in Model I and Model IIa; such diagrams induce a non-vanishing effective  $\mu_1$  even if this trilinear coupling is initially set to zero. The quark EDM and cEDMs are then induced at the three-loop level.

a divergent “bubble” diagram involving one  $g_2$  vertex and one  $g_1$  vertex, but  $g_2$  does not contribute to  $c_{10}$  at tree-level, so in the following discussion we will set  $g_2 = 0$ .

Inserting these one-loop triangle diagrams into the upper vertex of the EDM diagrams results in three-loop diagrams. Rather than performing the challenging full three-loop calculation, we use our earlier two-loop result for  $d_q$  and insert a lower bound on  $\mu_1$  due to the triangle diagrams:

$$\text{Model I: } \mu_1 \gtrsim \frac{g_1^3}{16\pi^2} \frac{m_S}{2m_\phi}, \quad (3.8)$$

$$\text{Model IIa: } \mu_1 \gtrsim \frac{\lambda_1^3}{16\pi^2} \frac{2m_\chi}{m_\phi}. \quad (3.9)$$

The relative factor of 4 accounts for the four degrees of freedom running in the loop in Model IIa; computationally it results from the Dirac trace appearing in the evaluation of the fermionic triangle diagram. In the next step, we convert this lower bound on  $\mu_1$  into a lower bound on the quark EDM (and cEDM) using eq.(2.22):

$$\text{Model I: } d_q \gtrsim \frac{e Q_q}{(16\pi^2)^3} (h_2 g_1)^3 m_S \lim_{q^2 \rightarrow 0} \left( [\mathcal{X}] + [\mathcal{Y}] \right); \quad (3.10)$$

$$\text{Model IIa: } d_q \gtrsim 4 \frac{e Q_q}{(16\pi^2)^3} (h_2 \lambda_1)^3 m_\chi \lim_{q^2 \rightarrow 0} \left( [\mathcal{X}] + [\mathcal{Y}] \right). \quad (3.11)$$

This leads directly to a lower bound on the nEDM, which can be translated into upper bounds on  $|h_2^3 g_1^3|$  and  $|h_2^3 \lambda_1^3|$  in Model I and Model IIa, respectively, by requiring our theoretical lower bound on  $d_n$  not exceed the stringent experimental upper bound.

Note that the products of couplings which are bounded by the nEDM also appear in the coefficient  $c_{10}$ , see eqs.(2.9) and (2.17), although with different powers: the bound on the nEDM scales cubically with the product of couplings whereas  $c_{10}$  scales linearly, i.e. the contribution from  $\mathcal{O}_{10}$  to the DM scattering rate scales quadratically. The same is true for

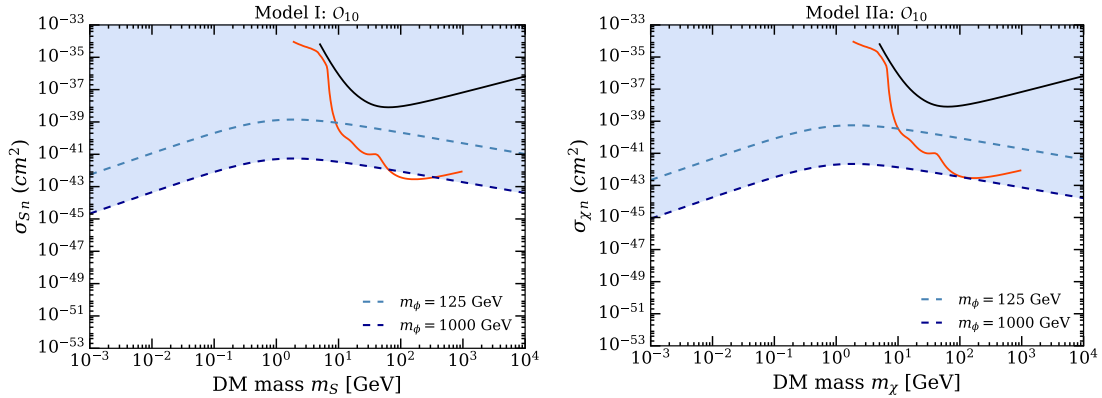


**Figure 10:** The **black** curves show the XENON1T upper bound on the DM–nucleon cross section from  $\mathcal{O}_{10}$  in Model I (left frame) and Model IIa (right frame) as a function of DM mass. The indirect constraint from the nEDM is shown by the **dashed light blue** curve for  $m_\phi = 125$  GeV and the **dashed dark blue** curve for  $m_\phi = 1000$  GeV; the shaded region is thus excluded by the nEDM bound for  $m_\phi = 1000$  GeV. The **red** curve denotes the neutrino floor for  $\mathcal{O}_{10}$  and has been taken from Ref. [68].

the “DM–nucleon scattering cross section” due to  $\mathcal{O}_{10}$ , defined by:

$$\sigma_{\mathcal{O}_{10}|^I} = \frac{3\mu_{SN}^2}{\pi} (c_{10|}^N|^I)^2 \quad \text{and} \quad \sigma_{\mathcal{O}_{10}|^{IIa}} = \frac{3\mu_{\chi N}^2}{\pi} (c_{10|}^N|^{IIa})^2. \quad (3.12)$$

The upper bounds on  $|h_2 g_1|$  and  $|h_2 \lambda_1|$  from the nEDM will thus lead to upper bounds on this cross section.

This is illustrated in Figs. 10, which show excluded regions in the plane spanned by  $\sigma_{\mathcal{O}_{10}}$  and the DM mass, for Model I (left) and Model IIa (right). The dashed blue curves depict the nEDM–derived 90% c.l. upper limit on the cross section for our two standard choices of the mediator mass  $m_\phi$ . This bound becomes weakest at DM mass  $m_{\text{DM}} \simeq 1$  GeV, i.e. close to the nucleon mass; here  $m_{\text{DM}} = m_S$  ( $m_\chi$ ) for Model I (Model IIa). For fixed couplings our estimated  $d_n$  of eq.(3.10) increases linearly with  $m_{\text{DM}}$ , while  $\sigma_{\mathcal{O}_{10}} \propto m_{\text{DM}}^2$  for  $m_{\text{DM}} \ll 1$  GeV but becomes independent of it for large DM mass. As a result, taking into account the different powers of couplings involved in the two quantities, the  $d_n$ –derived upper bound on  $\sigma_{\mathcal{O}_{10}}$  grows like  $m_{\text{DM}}^{4/3}$  for  $m_{\text{DM}} \ll 1$  GeV, but declines like  $m_{\text{DM}}^{-2/3}$  for  $m_{\text{DM}} \gg 1$  GeV. Moreover,  $\sigma_{\mathcal{O}_{10}} \propto m_\phi^{-4}$  while our estimated bound on  $d_n \propto m_\phi^{-2}$ ; the  $d_n$ –derived upper bound on  $\sigma_{\mathcal{O}_{10}}$  therefore scales  $\propto m_\phi^{-8/3}$  for all DM masses, i.e. the bound becomes more stringent for larger mediator mass. Finally, the bound is stronger in Model IIa by a factor of  $4^{2/3} \simeq 2.5$  due to the relative factor of 4 between the radiatively generated value of  $\mu_1$  given in eqs.(3.8).

The red curves in Fig. 10 show the irreducible background level from coherent neutrino–nucleus scattering (“neutrino floor”) as estimated in Ref. [68]. We see that the indirect constraint is around five orders of magnitude below the present XENON1T sensitivity, and for most DM masses well below the neutrino floor for  $m_\phi = 1000$  GeV. For this value of the mediator mass the current constraints on  $d_n$  therefore imply that the interactions due

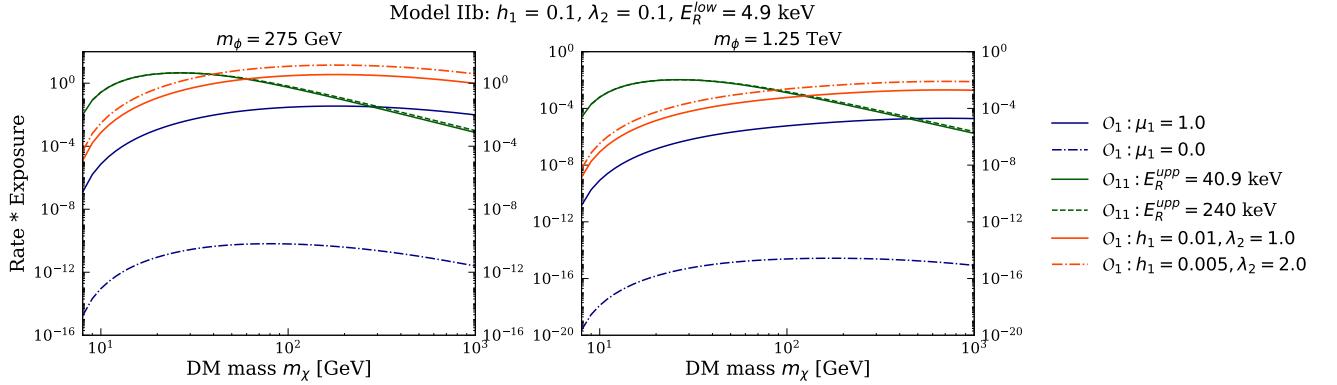


**Figure 11:** Total number of scattering events in Model IIb at XENON1T with a runtime exposure of 1 tonne–year as a function of the DM mass  $m_\chi$  for  $h_1 = \lambda_2 = 0.1$ , with  $m_\phi = 275 \text{ GeV}$  (left) and  $m_\phi = 1.25 \text{ TeV}$  (right). The **green** curves show the number of events due to  $\mathcal{O}_{11}$  and the **blue** curves show the number of events due to  $\mathcal{O}_1$ . The **red** curves also show contributions from  $\mathcal{O}_1$  with the same product  $h_1\lambda_2$ , and hence the same contribution from  $\mathcal{O}_{11}$ , but larger  $\lambda_2$ .

to  $\mathcal{O}_{10}$  are essentially unobservable; recall that for this large mediator mass,  $\mathcal{O}_1$  contributes even less to the scattering rate.

For  $m_\phi = 125 \text{ GeV}$ , the nEDM constraint still lies well below the current sensitivity. On the other hand, for  $m_{\text{DM}} \gtrsim 7 \text{ GeV}$  it is up to two orders of magnitude above the neutrino floor. Our analysis can therefore not completely exclude the possibility that future Xenon experiments might become sensitive to contributions from  $\mathcal{O}_{10}$ , if the upper bound on  $d_n$  remains unchanged. It should be noted, however, that saturating the bound on  $d_n$  requires relatively large couplings. Setting  $g_1 = \lambda_1 = 1$  and  $m_\phi = 125 \text{ GeV}$ , the estimate (3.10) is saturated for Yukawa coupling  $h_2 \simeq 0.13[m_\phi/(\kappa m_{\text{DM}})]^{1/3}$ , where  $\kappa = 1/2$  (2) in Model I (Model IIa); reducing the size of the DM–mediator coupling would require even larger  $h_2$ . Given our assumption of flavor–universal Yukawa couplings, experiments at LEP, the Tevatron and the LHC should be able to set quite stringent bounds on  $h_2$  for  $m_\phi \lesssim 125 \text{ GeV}$ . We finally discuss numerical results for Model IIb. We recall that this model had been constructed to generate the operator  $\mathcal{O}_{11}$  at tree–level, which is independent of the spin of the target nucleus. This required a scalar Yukawa coupling of the mediator to quarks, and a pseudoscalar coupling to the DM fermion. While this assignment quite manifestly again violates  $CP$ , it does not generate new contributions to the neutron EDM. However, at one–loop contributions to the leading spin–independent operator  $\mathcal{O}_1$  are generated also in this model.

In Figs. 11 and 12, we display the number of scattering events due to  $\mathcal{O}_1$  and  $\mathcal{O}_{11}$  for 1.0 tonne–year exposure of the XENON1T experiment as a function of the DM mass  $m_\chi$ . In each figure the mediator mass in the left frame is chosen such that the contribution from  $\mathcal{O}_{11}$  saturates the XENON1T constraint for  $m_\chi \simeq 30 \text{ GeV}$ , while in the right frame this contribution is barely above the neutrino floor for  $10 \text{ GeV} \lesssim m_\chi \lesssim 50 \text{ GeV}$  (and slightly below it for larger  $m_\chi$ ). We again assume flavor–universal Yukawa couplings  $h_1^q \equiv h_1$ . The

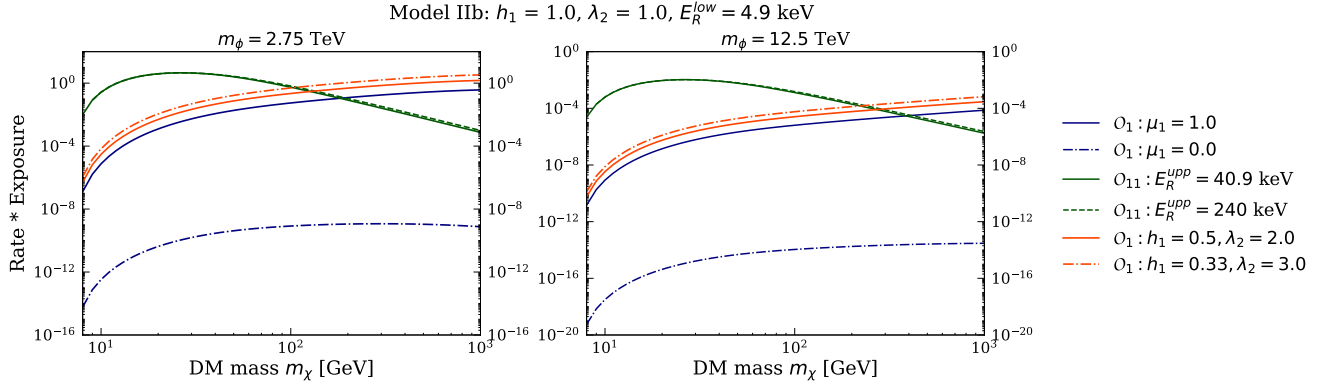


**Figure 12:** As in Fig. 11, but with  $\lambda_2 = h_1 = 1$  and correspondingly larger mediator masses:  $m_\phi = 2.75$  TeV (left) and  $m_\phi = 12.5$  TeV (right).

event rates due to  $\mathcal{O}_{11}$  are shown by the green lines, while the blue curves show the event rate due to  $\mathcal{O}_1$  for  $h_1 = \lambda_2 = 0.1$ , with ( $\mu_1 = 1$ , solid) or without ( $\mu_1 = 0$ , dashed) the triangle diagram. The red curves also show contribution due to  $\mathcal{O}_1$  with  $\mu_1 = 1$ , but for  $\lambda_2 > h_1$ , keeping the product  $\lambda_2 \cdot h_1$ , and hence the contribution from  $\mathcal{O}_{11}$ , constant.

Evidently the loop-induced contribution from  $\mathcal{O}_1$  can only be competitive if the triangle diagram is not suppressed. This is in accord with our discussion of eq.(2.20), which showed that this contribution is expected to dominate if  $\mu_1$  is sizable. We reiterate that there are logarithmically divergent one-loop contributions of order  $h_1^3 m_q / (16\pi^2 m_\phi)$  to this coupling from quark triangle diagrams, hence there is no reason to assume that  $\mu_1$  is very small.

We also see that in all cases the tree-level contribution from  $\mathcal{O}_{11}$  drops quickly for  $m_\chi \gtrsim 50$  GeV. This is partly due to the reduced flux of DM particles, which scales  $\propto 1/m_\chi$ , but mostly because  $c_{11} \propto 1/m_\chi$ , as shown in eq.(2.21). In contrast, the loop-induced contribution from  $\mathcal{O}_1$  in many cases keeps increasing with increasing  $m_\chi$  over the entire range shown. This is because for  $m_\chi \ll m_\phi$ , the triangle loop function satisfies  $sS_1(s) \simeq m_\chi / (2m_\phi^2)$ , hence this contribution to the scattering cross section scales  $\propto m_\chi^2$  for  $m_\chi \ll m_\phi$ . As a result, for  $\mu_1 = 1$  we always find that the contribution from  $\mathcal{O}_{11}$  dominates for small  $m_\chi$ , while that from  $\mathcal{O}_1$  is dominant at large  $m_\chi$ ; the DM mass where the two contributions are equal depends on the values of the other parameters. The behavior of the loop function  $S_1$  also explains why the contribution due to  $\mathcal{O}_1$  drops faster with increasing  $m_\phi$  than that due to  $\mathcal{O}_{11}$ , as long as  $m_\phi > m_\chi$ .

We note that the number of events from  $\mathcal{O}_{11}$  remains essentially unchanged when the maximal recoil energy is increased from 40.9 keV to 240 keV. As in case of  $\mathcal{O}_{10}$ , the scattering rate due to  $\mathcal{O}_{11}$  is peaked at non-zero recoil energies, due to the  $\vec{q}$  factor in the definition of this operator. However, unlike  $\mathcal{O}_{10}$ ,  $\mathcal{O}_{11}$  leads to coherent scattering on the entire nucleus. The rate is thus proportional to the square of the spin-independent elastic form factor of Xenon, which is quite soft. It is this coherent enhancement which leads to a much larger scattering rate from  $\mathcal{O}_{11}$  than from  $\mathcal{O}_{10}$ , for similar Wilson coefficients. However, the product of recoil energy  $E_R$  (which is  $\propto \vec{q}^2$ ) and squared form factor already peaks at  $E_R \simeq 20$  keV; the convolution with the DM velocity distribution further suppresses

the rate at large  $E_R$ .

Semi-quantitatively, the ratio of the two contributions can be estimated as follows:

$$\frac{N_{\mathcal{O}_1}}{N_{\mathcal{O}_{11}}}\Big|_{\text{IIb}} = \frac{R_{\mathcal{O}_1}}{R_{\mathcal{O}_{11}}}\Big|_{\text{IIb}} \sim \frac{(c_1^N|^{\text{IIb}})^2}{(c_{11}^N|^{\text{IIb}})^2} \frac{m_N^2}{\vec{q}^2}. \quad (3.13)$$

The nuclear response is the same for both contributions and therefore does not appear in the ratio. The factor  $(q^2/m_N^2)^{-1}$  is due to the momentum transfer dependence of  $\mathcal{O}_{11}$ . We only retain the leading triangle contribution to  $c_1^N|^{\text{IIb}}$ , see eq.(2.20),

$$c_1^N|^{\text{IIb}} \approx -\frac{\lambda_2^2}{16\pi^2} \mu_1 m_N \tilde{f}^N \frac{m_\chi}{m_\phi} S_1. \quad (3.14)$$

Using  $c_{11}^N|^{\text{IIb}}$  from eq.(2.21), the ratio of events is thus given by

$$\frac{N_{\mathcal{O}_1}}{N_{\mathcal{O}_{11}}}\Big|_{\text{IIb}} \approx \left( \frac{\lambda_2 \mu_1}{16\pi^2} \frac{m_\chi^2 m_\phi}{m_N} S_1(s) \right)^2 \frac{m_N}{2AE_R}. \quad (3.15)$$

For example, for  $\lambda_2 = \mu_1 = 1.0$ ,  $m_\phi = 2.75$  TeV and  $m_\chi = 200$  GeV, and taking  $E_R = 20$  keV as typical recoil energy in order to account for the soft form factor for coherent scattering, gives 0.45 for the ratio of event numbers, in rough agreement with the results shown in the left frame of Fig. 12. For the same couplings but increasing  $m_\phi$  to 12.5 TeV, eq.(3.15) predicts equal event rates for  $m_\chi = 520$  GeV, quite close to the intersection point between the green and blue lines in the right frame of Fig. 12. Moreover, eq.(3.15) also explains why increasing  $\lambda_2$  while keeping  $\lambda_2 \cdot h_1$  fixed (red curves) increases the contribution from  $\mathcal{O}_1$ . In fact, for  $m_\phi \lesssim 1$  TeV reducing  $h_1$  should help to avoid possible constraints on the model from searches at the LHC.

## 4 Summary and Conclusions

In this paper we explored the detection prospects involving  $P$ - and  $T$ -odd operators arising in the NREFT formalism of WIMP-nucleon scattering. These operators appear at next-to-leading order in an expansion in WIMP velocity  $v$  and momentum transfer  $\vec{q}$ . Since these quantities accompanying the  $P$ - and  $T$ -odd operators are quite small, these operators are expected to be insignificant relative to the leading order operators *if* the corresponding Wilson coefficients are of similar magnitude. Hence the additional operators can make significant contributions only when the coefficient of the leading spin-independent operator  $\mathcal{O}_1$  is strongly suppressed or vanishes entirely. This typically requires ad hoc choices of couplings in a relativistic QFT, i.e. one can generally not find a symmetry that suppresses the contribution from  $\mathcal{O}_1$  without also suppressing the Wilson coefficients of the additional operators.

Crucially, the  $P$ - and  $T$ -odd NREFT operators can only occur in the low energy limit of a QFT that violates the  $CP$  symmetry. This can lead to stringent constraints on the theory, in particular from electric dipole moments.

We addressed these concerns in the framework of three simplified models with uncharged  $t$ -channel mediators, taken from ref. [47]. These models extend the SM by a real scalar

mediator particle  $\phi$  which does not carry electric or color charge, and a DM particle which has spin 0 (Model I) or spin 1/2 (Model IIa and IIb). These models can generate flavor changing neutral currents already at tree-level unless the Yukawa couplings of the mediator are diagonal in the quark mass basis. This can easily be ensured if these new couplings are flavor-universal, which we therefore assumed in our numerical examples.

The couplings in these models are chosen such that at the lowest order in perturbation theory, only the  $P$ - and  $T$ -odd operators  $\mathcal{O}_{10}$  and  $\mathcal{O}_{11}$  arise in the non-relativistic limit. In particular,  $\phi$  must not have scalar couplings to both quarks and the DM particle. In Models I and IIa, the quark couplings are pseudoscalar while the DM couplings are scalar, while in Model IIb the quark couplings are scalar but the DM couplings are pseudoscalar. Note that there is no symmetry that forbids scalar quark couplings in Models I and IIa, or scalar DM couplings in Model IIb. It is therefore not surprising that at the next order in perturbation theory, one-loop box and triangle diagrams do induce the canonical SI interactions described by the operator  $\mathcal{O}_1$  in these models. We compared the tree-level interactions giving rise to  $\mathcal{O}_{10}$  or  $\mathcal{O}_{11}$  with the one-loop suppressed interactions yielding  $\mathcal{O}_1$ . To that end we computed the total number of events due to the two types of interactions for a Xenon target.

In the case of Model I and Model IIa and assuming large couplings in order to generate detectable event rates, we found that the contributions from  $\mathcal{O}_{10}$  can be roughly comparable to those from  $\mathcal{O}_1$  for mediator mass  $m_\phi = 125$  GeV, but for heavier mediator the contributions from  $\mathcal{O}_{10}$  clearly dominates. It thus appears as if  $\mathcal{O}_{10}$  could indeed be the most relevant NREFT operator in these models.

However, we pointed out that the quark-mediator interactions in both models produce two-loop contributions to  $d_n$ , the electric dipole moment of the neutron (nEDM). These contributions scale linearly with the cubic self-interaction of the mediator  $\mu_1$ . For parameter choices that lead to detectable event rates from  $\mathcal{O}_{10}$  and  $\mu_1$  of order unity (in units of  $m_\phi$ ), the predicted  $d_n$  is several orders of magnitude larger than the upper limit reported by experiments. Even if we set  $\mu_1 = 0$ , non-vanishing trilinear self-interactions are generated at one-loop level by couplings that also appear in the Wilson coefficient of  $\mathcal{O}_{10}$ . Estimating a lower bound on  $\mu_1$  from these loop diagrams, we find that the resulting upper bound on the WIMP-nucleus scattering rate is still well below current sensitivity, and often even below the irreducible background (“neutrino floor”), especially for large  $m_\phi$  where  $\mathcal{O}_{10}$  potentially dominates the scattering rate. As in case of models with charged,  $s$ -channel mediator, where  $d_n$  is generated already at one-loop level [50], it is thus essential to consider the  $d_n$  constraint when considering prospects for detecting WIMP-nucleus scattering due to  $\mathcal{O}_{10}$ . In Model IIb, which generates the spin-independent NREFT operator  $\mathcal{O}_{11}$ , we again found that the loop-induced contributions from  $\mathcal{O}_1$  can be larger than the tree-level contribution due to  $\mathcal{O}_{11}$ , if the trilinear scalar coupling  $\mu_1$  is not suppressed. We emphasized that in this model quark loops generate a logarithmically divergent one-loop contribution to  $\mu_1$ . For  $\mu_1 = 1$ ,  $\mathcal{O}_1$  typically dominates for large DM masses, while  $\mathcal{O}_{11}$  is dominant for small masses, the cross-over point depending on the values of the other parameters. In this model no new contributions to  $d_n$  are generated, and therefore this operator is not subject to the stringent constraints of the neutron EDM, even though it is also  $P$ - and  $T$ -odd.

At least at the level of a simplified model one can therefore engineer a scenario where the non-leading operator  $\mathcal{O}_{11}$  dominates the WIMP–nucleon scattering rate.

However, it is by no means clear whether this remains true in the framework of UV-complete theories. Recall that we only require our Lagrangians to be invariant under  $SU(3)_C \times U(1)_{em}$ ; we did not enforce invariance under the electroweak gauge symmetry. In particular, the  $\phi\bar{q}q$  couplings are not  $SU(2) \times U(1)_Y$  invariant if  $\phi$  is a singlet. The simplest choice would be to identify  $\phi$  with the Higgs boson of the SM, which resides in a doublet of  $SU(2)$ . However, the  $\phi\bar{q}q$  couplings are then known to be very small. Moreover, the WIMP can then also not be a gauge singlet, and would thus have additional (gauge) interactions leading to additional constraints as well as new contributions to WIMP–nucleon scattering. Alternatively one can couple a singlet WIMP to a singlet scalar which mixes with the SM Higgs boson; however, in such a scenario the WIMP–nucleon scattering rate would be suppressed even further by the mediator–Higgs mixing angle, which has to be rather small in order not to distort the properties of the physical 125 GeV particle too much.

We remind the reader that we assumed universal flavor–diagonal couplings of the mediator to the quarks. This simplifies the model building, since these couplings are then flavor–diagonal in any basis. On the other hand, it might appear more natural to assume that the new couplings increase with increasing quark mass, just as the Yukawa couplings of the SM do. In this case tree–level FCNC are avoided if the matrices of new Yukawa couplings commute with the Yukawa coupling matrices of the SM; from the model building point of view it is not clear why this should be the case. Moreover, keeping the couplings to the top quark  $\lesssim 1$  would then require very small couplings to the first generation. In such a scenario the contributions from heavy quarks might well dominate the DM scattering cross section, as well as – in Models I and IIa – the electric dipole moment of the neutron. In order to yield detectable event rates, the couplings to third generation quarks would have to be larger, and/or the mediator lighter, than in our numerical examples. It seems rather unlikely to us that this would lead to qualitatively different conclusions in Models I and IIa with unsuppressed trilinear self–coupling of the mediator, given the very large discrepancy between the predicted nEDM and its experimental upper bound that we found in our numerical examples; however, we have not performed an explicit computation to check this.<sup>10</sup>

In summary, the results presented in this paper as well as ref.[50] strongly indicate that the current experimental upper bound on the electric dipole moment of the neutron excludes the possibility that the operator  $\mathcal{O}_{10}$  can make contributions to WIMP–nucleus scattering to which current or near–future experiments are sensitive. While no such strong statement can be made for the operator  $\mathcal{O}_{11}$  generated by the exchange of a neutral mediator in the  $t$ –channel, it is currently unclear whether such a model can be constructed that respects the full gauge symmetry of the SM and leads to detectable WIMP–nucleon scattering being dominated by  $\mathcal{O}_{11}$ .

---

<sup>10</sup>The cEDMs of heavy quarks generate light quark cEDMs, as well as an electron EDM, at the three–loop level [69]. Moreover, the contribution of the gluonic Weinberg operator, which will generically be generated at three–loop level in Models I and IIa, would probably also have to be taken into account [70].



## Acknowledgments

We acknowledge the use of TikZ–Feynman [71] for creating Feynman diagrams and Package–X [72] for verifying parts of our loop computations. We thank Claude Duhr for discussions about the two loop diagram. RM was partially supported by the Bonn Cologne Graduate School of Physics and Astronomy.

## A 1-loop calculations

In this appendix we provide details of the calculations of the one–loop box and triangle diagrams appearing in Model I, IIa and IIb.

### A.1 Model I Matrix Element

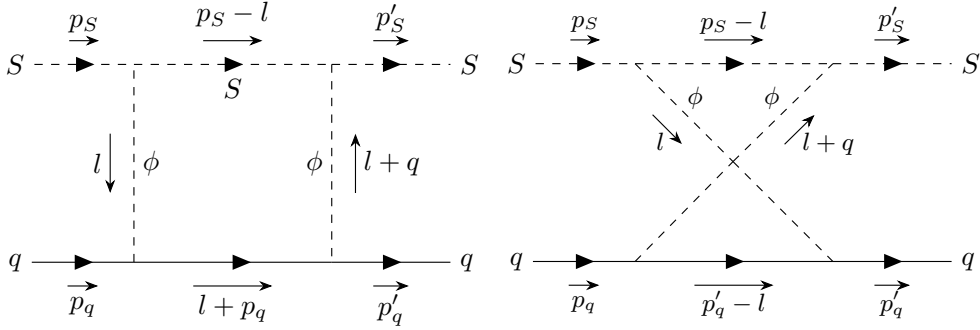


**Figure 13:** One-loop box and crossed box diagrams contributing to  $\mathcal{O}_1$  in Model I.

The box diagram shown in the left Fig. 13 gives the following contribution to the matrix element for DM–quark scattering:

$$i\mathcal{M}_1^I = (-ig_1 m_S)^2 \int \frac{d^4 l}{(2\pi)^4} \frac{i}{(p_S - l)^2 - m_S^2} \frac{i}{l^2 - m_\phi^2} \frac{i}{(l + q)^2 - m_\phi^2} \frac{i}{(p_q + l)^2 - m_q^2} \\ \times \bar{u}(p'_q) h_2^q \gamma^5 (\not{p}_q + \not{l} + m_q) h_2^q \gamma^5 u(p_q); \quad (\text{A.1})$$

the crossed box diagram shown in the right Fig. 13 contributes:

$$i\mathcal{M}_2^I = (-ig_1 m_S)^2 \int \frac{d^4 l}{(2\pi)^4} \frac{i}{(p_S - l)^2 - m_S^2} \frac{i}{l^2 - m_\phi^2} \frac{i}{(l + q)^2 - m_\phi^2} \frac{i}{(p'_q - l)^2 - m_q^2} \\ \times \bar{u}(p'_q) h_2^q \gamma^5 (\not{p}'_q - \not{l} + m_q) h_2^q \gamma^5 u(p_q). \quad (\text{A.2})$$

After simplifying the numerator by commuting the two  $\gamma^5$  matrices and using the Dirac equation, we obtain for the two diagrams:

$$i\mathcal{M}_1^I = g_1^2 (h_2^q)^2 m_S^2 M_{1,\mu}^I \bar{u}(p'_q) \gamma^\mu u(p_q) \quad \text{and} \quad (\text{A.3})$$

$$i\mathcal{M}_2^I = -g_1^2 (h_2^q)^2 m_S^2 M_{2,\mu}^I \bar{u}(p'_q) \gamma^\mu u(p_q). \quad (\text{A.4})$$

Here  $M_{1,\mu}^I$  and  $M_{2,\mu}^I$  are loop integrals:

$$M_{1,\mu}^I = \int \frac{d^4l}{(2\pi)^4} \frac{l_\mu}{[(p_S - l)^2 - m_S^2] [l^2 - m_\phi^2] [(l + q)^2 - m_\phi^2] [(p_q + l)^2 - m_q^2]}, \quad (\text{A.5})$$

$$M_{2,\mu}^I = \int \frac{d^4l}{(2\pi)^4} \frac{l_\mu}{[(p_S - l)^2 - m_S^2] [l^2 - m_\phi^2] [(l + q)^2 - m_\phi^2] [(p'_q - l)^2 - m_q^2]}. \quad (\text{A.6})$$

After Feynman parametrization, these loop integrals can be expressed in the vanishing momentum transfer limit ( $q \rightarrow 0$ , i.e.  $p_S \rightarrow p'_S$  and  $p_q \rightarrow p'_q$ ) in terms of loop functions  $M_i(r = m_q/m_\phi, s = m_S/m_\phi)$ ,  $i = 1, \dots, 4$ , which are given in Appendix A.1.1. The contributions from the box diagram and crossed box diagrams can then finally be written as:

$$\mathcal{M}_1^I = \frac{(h_2^q)^2 g_1^2 m_S^2}{16\pi^2} \left[ \left( \frac{p_{S,\mu} + p'_{S,\mu}}{2} \right) M_1 \bar{u}(p'_q) \gamma^\mu u(p_q) + m_q M_2 \bar{u}(p'_q) u(p_q) \right], \quad (\text{A.7})$$

$$\mathcal{M}_2^I = - \frac{(h_2^q)^2 g_1^2 m_S^2}{16\pi^2} \left[ \left( \frac{p_{S,\mu} + p'_{S,\mu}}{2} \right) M_3 \bar{u}(p'_q) \gamma^\mu u(p_q) - m_q M_4 \bar{u}(p'_q) u(p_q) \right]. \quad (\text{A.8})$$

Even though  $p_S = p'_S$  for  $q = 0$  we've written these contributions in terms of the symmetric sum  $p_S + p'_S$ , which facilitates matching onto the effective Lagrangian of eq.(2.5) after integrating out the mediator.

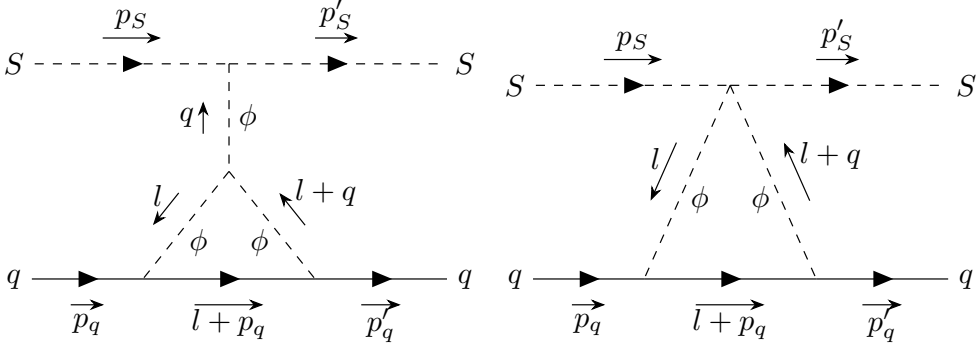


**Figure 14:** One-loop triangle diagrams contributing to  $\mathcal{O}_1$  in Model I.

Fig. 14 shows contributions to WIMP–quark scattering in Model I from triangle diagrams. The matrix element for the left diagram reads:

$$i\mathcal{M}_{\Delta_1}^I = (-im_\phi \mu_1) (-ig_1 m_S) \frac{i}{q^2 - m_\phi^2} \int \frac{d^4l}{(2\pi)^4} \frac{i}{l^2 - m_\phi^2} \frac{i}{(l + q)^2 - m_\phi^2} \frac{i}{(p_q + l)^2 - m_q^2} \\ \times \bar{u}(p'_q) h_2^q \gamma^5 (\not{p}_q + \not{l} + m_q) h_2^q \gamma^5 u(p_q); \quad (\text{A.9})$$

the right triangle diagram contributes:

$$i\mathcal{M}_{\Delta_2}^I = \left( \frac{-ig_2}{2} \right) \int \frac{d^4l}{(2\pi)^4} \frac{i}{l^2 - m_\phi^2} \frac{i}{(l + q)^2 - m_\phi^2} \frac{i}{(p_q + l)^2 - m_q^2} \\ \times \bar{u}(p'_q) h_2^q \gamma^5 (\not{p}_q + \not{l} + m_q) h_2^q \gamma^5 u(p_q). \quad (\text{A.10})$$

Again commuting the two  $\gamma^5$  matrices and using the Dirac equation, we obtain for these two diagrams:

$$i\mathcal{M}_{\Delta_1}^I = g_1\mu_1(h_2^q)^2 \frac{m_S m_\phi}{q^2 - m_\phi^2} M_{3,\mu}^I \bar{u}(p'_q)\gamma^\mu u(p_q) \quad \text{and} \quad (\text{A.11})$$

$$i\mathcal{M}_{\Delta_2}^I = \frac{g_2}{2}(h_2^q)^2 M_{3,\mu}^I \bar{u}(p'_q)\gamma^\mu u(p_q) . \quad (\text{A.12})$$

The loop integral  $M_{3,\mu}^I$  is:

$$M_{3,\mu}^I = \int \frac{d^4l}{(2\pi)^4} \frac{l_\mu}{[l^2 - m_\phi^2] [(l+q)^2 - m_\phi^2] [(p_q+l)^2 - m_q^2]} . \quad (\text{A.13})$$

In the limit  $q \rightarrow 0$  it can be expressed in terms of the loop function  $L_1$ , whose analytic expression is given in Appendix A.1.1. The contribution of the two triangle diagrams to the matrix element can then finally be written as

$$\mathcal{M}_{\Delta_1}^I = \frac{g_1\mu_1(h_2^q)^2}{16\pi^2} \frac{m_q m_S}{m_\phi} L_1(m_q^2, m_\phi^2) \bar{u}(p'_q) u(p_q) , \quad (\text{A.14})$$

$$\mathcal{M}_{\Delta_2}^I = -\frac{g_2(h_2^q)^2}{16\pi^2} \frac{m_q}{2} L_1(m_q^2, m_\phi^2) \bar{u}(p'_q) u(p_q) . \quad (\text{A.15})$$

### A.1.1 Model I Loop Functions

We first define the function  $L(x)$  of the real variable  $x$  as:

$$L(x) = \begin{cases} \sqrt{1-4x^2} \cdot \ln\left(\frac{1+\sqrt{1-4x^2}}{2|x|}\right) & \text{for } |x| \leq 0.5 \\ -\sqrt{4x^2-1} \cdot \arctan\left(\sqrt{4x^2-1}\right) & \text{for } |x| \geq 0.5 \end{cases} . \quad (\text{A.16})$$

In terms of this function, the loop functions  $M_i$ ,  $i = 1, \dots, 4$  and  $L_1$  can be written as:

$$M_1 = \frac{1}{3m_\phi^4} \left[ \frac{1}{s(r+s)} - \frac{(1+2r^2)}{2r^2(r+s)^2} L(r) + \frac{s-2r}{4r^2s^3} \ln(1/s^2) - \frac{\ln(r^2/s^2)}{4r^2(r+s)^2} + \frac{2r+3s-4rs^2-6s^3+8rs^4}{2s^3(r+s)^2(1-4s^2)} L(s) \right]; \quad (\text{A.17})$$

$$M_2 = \frac{1}{3m_\phi^4} \left[ -\frac{1}{r(r+s)} + \frac{1+2s^2}{2s^2(r+s)^2} L(s) - \frac{r-2s}{4r^3s^2} \ln(1/s^2) - \frac{(3r+2s)\ln(r^2/s^2)}{4r^3(r+s)^2} + \frac{2s+3r-4r^2s-6r^3+8r^4s}{2r^3(4r^2-1)(r+s)^2} L(r) \right]; \quad (\text{A.18})$$

$$M_3 = \frac{1}{3m_\phi^4} \left[ \frac{1}{s(s-r)} - \frac{1+2r^2}{2r^2(r-s)^2} L(r) + \frac{s+2r}{4r^2s^3} \ln(1/s^2) - \frac{\ln(r^2/s^2)}{4r^2(r-s)^2} - \frac{2r-3s-4rs^2+6s^3+8rs^4}{2s^3(r-s)^2(1-4s^2)} L(s) \right]; \quad (\text{A.19})$$

$$M_4 = \frac{1}{3m_\phi^4} \left[ -\frac{1}{r(r-s)} + \frac{1+2s^2}{2s^2(r-s)^2} L(s) - \frac{r+2s}{4r^3s^2} \ln(1/s^2) - \frac{(3r-2s)\ln(r^2/s^2)}{4r^3(r-s)^2} + \frac{2s-3r-4r^2s+6r^3+8r^4s}{2r^3(1-4r^2)(r-s)^2} L(r) \right]; \quad (\text{A.20})$$

$$L_1 = \frac{1}{m_\phi^2} \left[ \frac{1}{r^2} + \frac{r^2-1}{2r^4} \ln(1/r^2) + \frac{1-3r^2}{r^4(1-4r^2)} L(r) \right]. \quad (\text{A.21})$$

We note that  $M_3(r, s) = M_1(-r, s) = M_1(r, -s)$  and  $M_4(r, s) = M_2(-r, s) = M_2(r, -s)$ , i.e. the functions  $M_i$  remain invariant when both arguments change their sign. Of course, in our application only positive arguments are physical, since  $r = m_q/m_\phi$  and  $s = m_S/m_\phi$ . In our examples we assume flavor-universal Yukawa couplings. In this case the contribution from the light quarks will dominate the WIMP-nucleon scattering matrix elements. We therefore also give the **massless quark limits of the loop functions**:

$$M_1, M_3 \xrightarrow{r \rightarrow 0} \frac{1}{2m_\phi^4} \frac{1}{s^2} \left[ 1 - \frac{1}{2s^2} \ln\left(\frac{1}{s^2}\right) + \frac{1-2s^2}{s^2(1-4s^2)} L(s) \right]; \quad (\text{A.22})$$

$$M_2, M_4 \xrightarrow{r \rightarrow 0} \frac{1}{6m_\phi^4} \frac{1}{s^2} \left[ 1 - \frac{1}{2s^2} \ln\left(\frac{1}{s^2}\right) + \frac{1+2s^2}{s^2} L(s) \right]; \quad (\text{A.23})$$

$$L_1 \xrightarrow{r \rightarrow 0} -\frac{1}{2m_\phi^2}. \quad (\text{A.24})$$

## A.2 Model IIa and IIb Matrix Elements

We now turn to the models with fermionic WIMP  $\chi$ . We again begin with the box and crossed box diagrams shown in Fig. 15. The contribution to the matrix element for DM-quark scattering from the box diagram in Model IIa, involving the scalar DM-mediator

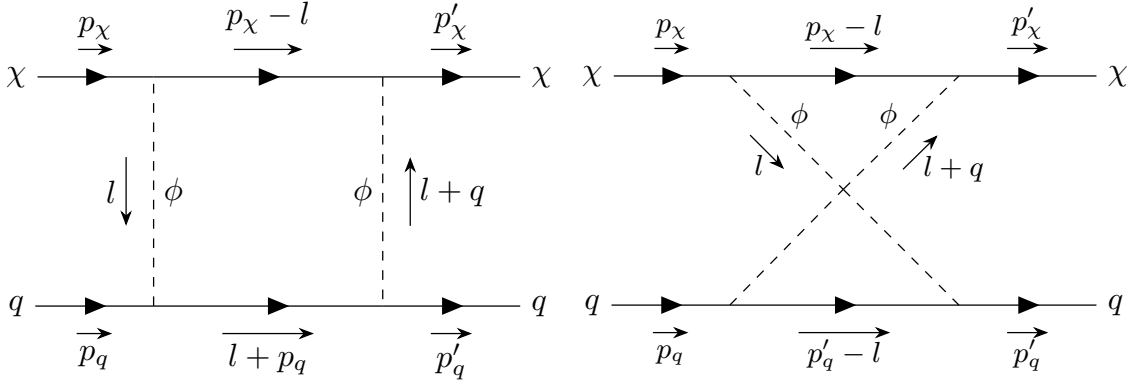


**Figure 15:** One-loop box diagrams contributing to  $\mathcal{O}_1$  in Model IIa or Model IIb.

coupling  $\lambda_1$ , is

$$i\mathcal{M}_1^{\text{IIa}} = (-i\lambda_1)^2 \int \frac{d^4l}{(2\pi)^4} \frac{i}{(p_\chi - l)^2 - m_\chi^2} \frac{i}{l^2 - m_\phi^2} \frac{i}{(l + q)^2 - m_\phi^2} \frac{i}{(p_q + l)^2 - m_\phi^2} \\ \times \bar{u}(p'_\chi)(\not{p}_\chi - \not{l} + m_\chi)u(p_\chi)\bar{u}(p'_q)h_2^q\gamma^5(\not{p}_q + \not{l} + m_q)h_2^q\gamma^5u(p_q); \quad (\text{A.25})$$

the crossed box diagram contributes:

$$i\mathcal{M}_2^{\text{IIa}} = (-i\lambda_1)^2 \int \frac{d^4l}{(2\pi)^4} \frac{i}{(p_\chi - l)^2 - m_\chi^2} \frac{i}{l^2 - m_\phi^2} \frac{i}{(l + q)^2 - m_\phi^2} \frac{i}{(p'_q - l)^2 - m_\phi^2} \\ \times \bar{u}(p'_\chi)(\not{p}_\chi - \not{l} + m_\chi)u(p_\chi)\bar{u}(p'_q)h_2^q\gamma^5(\not{p}'_q - \not{l} + m_q)h_2^q\gamma^5u(p_q). \quad (\text{A.26})$$

After simplifying the numerator by commuting the two  $\gamma^5$  matrices and using the Dirac equation for the external quarks and WIMPs, we obtain for the two diagrams:

$$i\mathcal{M}_1^{\text{IIa}} = -\lambda_1^2 (h_2^q)^2 \left( N_{1,\mu\nu}^{\text{IIa}} [\bar{u}(p'_q)\gamma^\mu u(p_q)] [\bar{u}(p'_\chi)\gamma^\nu u(p_\chi)] \right. \\ \left. - 2m_\chi N_{2,\mu}^{\text{IIa}} [\bar{u}(p'_q)\gamma^\mu u(p_q)] [\bar{u}(p'_\chi)u(p_\chi)] \right); \quad (\text{A.27})$$

$$i\mathcal{M}_2^{\text{IIa}} = \lambda_1^2 (h_2^q)^2 \left( N_{3,\mu\nu}^{\text{IIa}} [\bar{u}(p'_q)\gamma^\mu u(p_q)] [\bar{u}(p'_\chi)\gamma^\nu u(p_\chi)] \right. \\ \left. - 2m_\chi N_{4,\mu}^{\text{IIa}} [\bar{u}(p'_q)\gamma^\mu u(p_q)] [\bar{u}(p'_\chi)u(p_\chi)] \right). \quad (\text{A.28})$$

Here  $N_{1,\mu\nu}^{\text{IIa}}$ ,  $N_{3,\mu\nu}^{\text{IIa}}$ ,  $N_{3,\mu}^{\text{IIa}}$  and  $N_{4,\mu}^{\text{IIa}}$  are loop integrals:

$$N_{1,\mu\nu}^{\text{IIa}} = \int \frac{d^4l}{(2\pi)^4} \frac{l_\mu l_\nu}{[(p_\chi - l)^2 - m_\chi^2] [l^2 - m_\phi^2] [(l + q)^2 - m_\phi^2] [(p_q + l)^2 - m_\phi^2]}; \quad (\text{A.29})$$

$$N_{2,\mu}^{\text{IIa}} = \int \frac{d^4l}{(2\pi)^4} \frac{l_\mu}{[(p_\chi - l)^2 - m_\chi^2] [l^2 - m_\phi^2] [(l + q)^2 - m_\phi^2] [(p_q + l)^2 - m_\phi^2]}; \quad (\text{A.30})$$

$$N_{3,\mu\nu}^{\text{IIa}} = \int \frac{d^4l}{(2\pi)^4} \frac{l_\mu l_\nu}{[(p_\chi - l)^2 - m_\chi^2] [l^2 - m_\phi^2] [(l + q)^2 - m_\phi^2] [(p'_q - l)^2 - m_\phi^2]}; \quad (\text{A.31})$$

$$N_{4,\mu}^{\text{IIa}} = \int \frac{d^4l}{(2\pi)^4} \frac{l_\mu}{[(p_\chi - l)^2 - m_\chi^2] [l^2 - m_\phi^2] [(l + q)^2 - m_\phi^2] [(p'_q - l)^2 - m_\phi^2]}. \quad (\text{A.32})$$

After Feynman parametrization and taking the limit  $q \rightarrow 0$ , the loop integrals in eqs.(A.29) to (A.32) can be expressed in terms of loop functions  $N_i$ ,  $i = 1, \dots, 8$  and  $P_j$ ,  $j = 1, \dots, 4$  whose analytic expressions can be found in Appendix A.2.1. Both sets of functions depend on  $r = m_q/m_\phi$  and  $s = m_\chi/m_\phi$ . The contributions from the box and crossed box diagrams can then be written as:

$$\begin{aligned} \mathcal{M}_1^{\text{IIa}} = & -\frac{\lambda_1^2 (h_2^q)^2}{16 \pi^2} \left\{ N_1 [\bar{u}(p'_\chi) \gamma^\mu \bar{u}(p_\chi)] [\bar{u}(p'_q) \gamma_\mu u(p_q)] \right. \\ & + \left( 2m_\chi m_q (N_2 - P_2) + m_\chi^2 (N_3 - 2P_1) + m_q^2 N_4 \right) \\ & \left. \times [\bar{u}(p'_\chi) \bar{u}(p_\chi)] [\bar{u}(p'_q) u(p_q)] \right\}; \end{aligned} \quad (\text{A.33})$$

$$\begin{aligned} \mathcal{M}_2^{\text{IIa}} = & \frac{\lambda_1^2 (h_2^q)^2}{16 \pi^2} \left\{ N_5 [\bar{u}(p'_\chi) \gamma^\mu \bar{u}(p_\chi)] [\bar{u}(p'_q) \gamma_\mu u(p_q)] \right. \\ & + \left( 2m_\chi m_q (N_6 - P_4) + m_\chi^2 (N_7 - 2P_3) + m_q^2 N_8 \right) \\ & \left. \times [\bar{u}(p'_\chi) \bar{u}(p_\chi)] [\bar{u}(p'_q) u(p_q)] \right\}. \end{aligned} \quad (\text{A.34})$$

The diagrams of Fig. 15 also contribute when both DM–mediator couplings are  $\lambda_2$ . The contribution from the box diagram reads:

$$\begin{aligned} i\mathcal{M}_3^{\text{IIa}} = & \lambda_2^2 (h_2^q)^2 \int \frac{d^4 l}{(2\pi)^4} \frac{i}{(p_\chi - l)^2 - m_\chi^2} \frac{i}{l^2 - m_\phi^2} \frac{i}{(l + q)^2 - m_\phi^2} \frac{i}{(p_q + l)^2 - m_q^2} \\ & \times \bar{u}(p'_\chi) \gamma^5 (\not{p}_\chi - \not{l} + m_\chi) \gamma^5 u(p_\chi) \bar{u}(p'_q) \gamma^5 (\not{p}_q + \not{l} + m_q) \gamma^5 u(p_q). \end{aligned} \quad (\text{A.35})$$

The crossed box contributes:

$$\begin{aligned} i\mathcal{M}_4^{\text{IIa}} = & \lambda_2^2 (h_2^q)^2 \int \frac{d^4 l}{(2\pi)^4} \frac{i}{(p_\chi - l)^2 - m_\chi^2} \frac{i}{l^2 - m_\phi^2} \frac{i}{(l + q)^2 - m_\phi^2} \frac{i}{(p'_q - l)^2 - m_q^2} \\ & \times \bar{u}(p'_\chi) \gamma^5 (\not{p}_\chi - \not{l} + m_\chi) \gamma^5 u(p_\chi) \bar{u}(p'_q) \gamma^5 (\not{p}'_q - \not{l} + m_q) \gamma^5 u(p_q). \end{aligned} \quad (\text{A.36})$$

After commuting the two  $\gamma^5$  matrices and using the Dirac equation, these simplify to

$$i\mathcal{M}_3^{\text{IIa}} = -\lambda_2^2 (h_2^q)^2 N_{1,\mu\nu}^{\text{IIa}} [\bar{u}(p'_q) \gamma^\mu u(p_q)] [\bar{u}(p'_\chi) \gamma^\nu u(p_\chi)]; \quad (\text{A.37})$$

$$i\mathcal{M}_4^{\text{IIa}} = \lambda_2^2 (h_2^q)^2 N_{3,\mu\nu}^{\text{IIa}} [\bar{u}(p'_q) \gamma^\mu u(p_q)] [\bar{u}(p'_\chi) \gamma^\nu u(p_\chi)], \quad (\text{A.38})$$

where  $N_{1,\mu\nu}^{\text{IIa}}$  and  $N_{3,\mu\nu}^{\text{IIa}}$  are loop integrals defined in eqs.(A.29) and (A.31). In the  $q \rightarrow 0$  limit we finally obtain:

$$\begin{aligned} \mathcal{M}_3^{\text{IIa}} = & -\frac{\lambda_2^2 (h_2^q)^2}{16 \pi^2} \left\{ N_1 [\bar{u}(p'_\chi) \gamma^\mu \bar{u}(p_\chi)] [\bar{u}(p'_q) \gamma_\mu u(p_q)] \right. \\ & \left. + (2m_\chi m_q N_2 + m_\chi^2 N_3 + m_q^2 N_4) [\bar{u}(p'_\chi) \bar{u}(p_\chi)] [\bar{u}(p'_q) u(p_q)] \right\}; \end{aligned} \quad (\text{A.39})$$

$$\begin{aligned} \mathcal{M}_4^{\text{IIa}} = & \frac{\lambda_2^2 (h_2^q)^2}{16 \pi^2} \left\{ N_5 [\bar{u}(p'_\chi) \gamma^\mu \bar{u}(p_\chi)] [\bar{u}(p'_q) \gamma_\mu u(p_q)] \right. \\ & \left. + (2m_\chi m_q N_6 + m_\chi^2 N_7 + m_q^2 N_8) [\bar{u}(p'_\chi) \bar{u}(p_\chi)] [\bar{u}(p'_q) u(p_q)] \right\}. \end{aligned} \quad (\text{A.40})$$

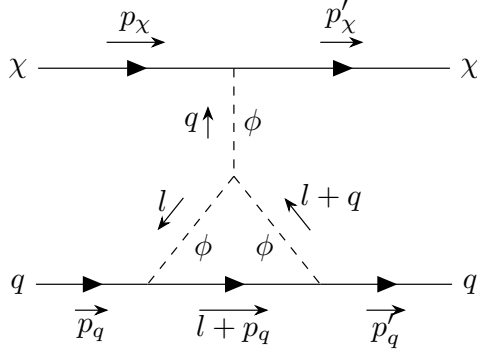


**Figure 16:** One-loop triangle diagram contributing to  $\mathcal{O}_1$  in Model IIa involving the couplings  $\lambda_1$ ,  $\mu_1$  and  $h_2^q$ .

The functions  $N_i$  already appeared in the contributions  $\propto \lambda_1^2$ ; they are defined in Appendix A.2.1. This completes the contribution from the diagrams of Fig 15, since diagrams involving one scalar and one pseudoscalar coupling on the WIMP line do not contribute to  $\mathcal{O}_1$ .

There is only one triangle diagram contributing to  $\mathcal{O}_1$  at one-loop order in Model IIa, as shown in Fig. 16; note that only the diagram involving the scalar DM-mediator coupling  $\lambda_1$  contributes to  $\mathcal{O}_1$ . Its contribution to the DM-quark scattering matrix element is given by:

$$i\mathcal{M}_{\Delta}^{\text{IIa}} = \frac{i(-i\lambda_1)(-im_\phi\mu_1)}{q^2 - m_\phi^2} \int \frac{d^4l}{(2\pi)^4} \frac{i}{l^2 - m_\phi^2} \frac{i}{(l+q)^2 - m_\phi^2} \frac{i}{(l+q)^2 - m_\phi^2} \quad (\text{A.41})$$

$$\times [\bar{u}(p'_\chi) u(p_\chi)] \bar{u}(p'_q) h_2^q \gamma^5 (\not{p}_q + \not{l} + m_q) h_2^q \gamma^5 u(p_q). \quad (\text{A.42})$$

After simplifying the numerator as before, we get:

$$\mathcal{M}_{\Delta}^{\text{IIa}} = -\frac{\lambda_1 (h_2^q)^2 \mu_1}{16 \pi^2} \left( \frac{m_q}{m_\phi} \right) R_1 [\bar{u}(p'_\chi) u(p_\chi)] [\bar{u}(p'_q) u(p_q)]. \quad (\text{A.43})$$

Here a new loop function  $R_1$  appears, which is also defined in Appendix A.2.1.

The calculations for Model IIb are very similar. The (crossed) box diagrams look exactly the same as in Model IIa, but now we have scalar Yukawa couplings on the quark line and pseudoscalar couplings on the WIMP line. We only list the final results. For the box and crossed box we obtain:

$$\begin{aligned} \mathcal{M}_1^{\text{IIb}} = & -\frac{\lambda_2^2 (h_1^q)^2}{16 \pi^2} \left[ N_1 [\bar{u}(p'_\chi) \gamma^\mu \bar{u}(p_\chi)] [\bar{u}(p'_q) \gamma_\mu u(p_q)] \right. \\ & + (2m_\chi m_q (N_2 + P_1) + m_\chi^2 N_3 + m_q^2 (N_4 + 2P_2)) \\ & \left. \times [\bar{u}(p'_\chi) \bar{u}(p_\chi)] [\bar{u}(p'_q) u(p_q)] \right] \quad (\text{A.44}) \end{aligned}$$

$$\begin{aligned} \mathcal{M}_2^{\text{IIb}} = & \frac{\lambda_2^2 (h_1^q)^2}{16 \pi^2} \left[ N_5 [\bar{u}(p'_\chi) \gamma^\mu \bar{u}(p_\chi)] [\bar{u}(p'_q) \gamma_\mu u(p_q)] \right. \\ & + (2m_\chi m_q (N_6 - P_3) + m_\chi^2 N_7 + m_q^2 (N_8 - 2P_4)) \\ & \left. \times [\bar{u}(p'_\chi) \bar{u}(p_\chi)] [\bar{u}(p'_q) u(p_q)] \right]. \quad (\text{A.45}) \end{aligned}$$

The functions  $N_i$  and  $P_k$  are the same as in Model IIa, and are defined in Appendix A.2.1. The Model IIb triangle diagram shown in Fig. 3 yields:

$$\mathcal{M}_{\Delta}^{\text{IIb}} = -\frac{h_1^q \lambda_2^2 \mu_1}{16 \pi^2} \left( \frac{m_\chi}{m_\phi} \right) S_1 [\bar{u}(p'_\chi) u(p_\chi)] [\bar{u}(p'_q) u(p_q)] . \quad (\text{A.46})$$

Here a new loop function  $S_1$  appears; it is also defined in Appendix A.2.1.

### A.2.1 Model IIa and IIb Loop Functions

These functions are again expressed in terms of the function  $L(x)$  defined in eq.(A.16).

$$N_1 = -\frac{1}{6 m_\phi^2} \left[ \frac{1}{rs} - \frac{r^2 - 1}{r^3(r+s)} L(r) + \frac{rs - s^2 + r^2(3s^2 - 1)}{2r^3 s^3} \ln\left(\frac{1}{s^2}\right) + \frac{1 - 3r^2}{2r^3(r+s)} \ln\left(\frac{r^2}{s^2}\right) - \frac{s^2 - 1}{s^3(r+s)} L(s) \right]; \quad (\text{A.47})$$

$$N_2 = \frac{1}{30 m_\phi^4} \left[ \frac{3r^2 + 2rs + 3s^2 - 8r^2 s^2}{r^2 s^2 (r+s)^2} + \frac{5r - 5r^3 + 3s + r^2 s + 8r^4 s}{r^4 (r+s)^3} L(r) + \frac{-3r^2 + 4rs - 3s^2 + 5r^2 s^2}{2r^4 s^4} \ln\left(\frac{1}{s^2}\right) + \frac{5r - 15r^3 + 3s - 5r^2 s}{2r^4 (r+s)^3} \ln\left(\frac{r^2}{s^2}\right) + \frac{3r + 5s + rs^2 - 5s^3 + 8rs^4}{s^4 (r+s)^3} L(s) \right]; \quad (\text{A.48})$$

$$N_3 = \frac{1}{15 m_\phi^4} \left[ \frac{6r^2 + 9rs + s^2 + 4r^2 s^2}{rs^3 (r+s)^2} + \frac{1 - 3r^2 - 4r^4}{r^3 (r+s)^3} L(r) + \frac{-6r^2 + 3rs - s^2 + 5r^2 s^2}{2r^3 s^5} \ln\left(\frac{1}{s^2}\right) + \frac{1 - 5r^2}{2r^3 (r+s)^3} \ln\left(\frac{r^2}{s^2}\right) + \frac{6r^2 + 15rs + 10s^2 - 17r^2 s^2 - 45rs^3 - 35s^4 - 2r^2 s^4 + 10s^6 + 16r^2 s^6}{s^5 (r+s)^3 (1 - 4s^2)} L(s) \right]; \quad (\text{A.49})$$

$$N_4 = \frac{1}{15 m_\phi^4} \left[ \frac{r^2 + 9rs + 6s^2 + 4r^2 s^2}{r^3 s (r+s)^2} + \frac{-r^2 + 3rs - 6s^2 + 5r^2 s^2}{2r^5 s^3} \ln\left(\frac{1}{r^2}\right) + \frac{10r^2 - 35r^4 + 10r^6 + 15rs - 45r^3 s + 6s^2 - 17r^2 s^2 - 2r^4 s^2 + 16r^6 s^2}{r^5 (1 - 4r^2) (r+s)^3} L(r) + \frac{-1 + 5s^2}{2s^3 (r+s)^3} \ln\left(\frac{r^2}{s^2}\right) + \frac{1 - 3s^2 - 4s^4}{s^3 (r+s)^3} L(s) \right]; \quad (\text{A.50})$$

$$N_5 = \frac{1}{6 m_\phi^2} \left[ \frac{1}{rs} - \frac{1 - r^2}{r^3 (r-s)} L(r) + \frac{-r^2 - rs - s^2 + 3r^2 s^2}{2r^3 s^3} \ln\left(\frac{1}{s^2}\right) + \frac{-1 + 3r^2}{2r^3 (r-s)} \ln\left(\frac{r^2}{s^2}\right) - \frac{1 - s^2}{s^3 (-r+s)} L(s) \right]; \quad (\text{A.51})$$



$$\begin{aligned}
N_6 = \frac{1}{30 m_\phi^4} & \left[ -\frac{3r^2 - 2rs + 3s^2 - 8r^2s^2}{r^2s^2(r-s)^2} - \frac{5r - 5r^3 - 3s - r^2s - 8r^4s}{r^4(r-s)^3} \text{L}(r) \right. \\
& + \frac{3r^2 + 4rs + 3s^2 - 5r^2s^2}{2r^4s^4} \ln\left(\frac{1}{s^2}\right) + \frac{-5r + 15r^3 + 3s - 5r^2s}{2r^4(r-s)^3} \ln\left(\frac{r^2}{s^2}\right) \\
& \left. - \frac{3r - 5s + rs^2 + 5s^3 + 8rs^4}{s^4(r-s)^3} \text{L}(s) \right]; \tag{A.52}
\end{aligned}$$

$$\begin{aligned}
N_7 = \frac{1}{15 m_\phi^4} & \left[ -\frac{6r^2 - 9rs + s^2 + 4r^2s^2}{rs^3(r-s)^2} + \frac{1 - 3r^2 - 4r^4}{r^3(r-s)^3} \text{L}(r) \right. \\
& + \frac{6r^2 + 3rs + s^2 - 5r^2s^2}{2r^3s^5} \ln\left(\frac{1}{s^2}\right) + \frac{1 - 5r^2}{2r^3(r-s)^3} \ln\left(\frac{r^2}{s^2}\right) \\
& \left. - \frac{6r^2 - 15rs + 10s^2 - 17r^2s^2 + 45rs^3 - 35s^4 - 2r^2s^4 + 10s^6 + 16r^2s^6}{s^5(r-s)^3(1-4s^2)} \text{L}(s) \right]; \tag{A.53}
\end{aligned}$$

$$\begin{aligned}
N_8 = \frac{1}{15 m_\phi^4} & \left[ -\frac{r^2 - 9rs + 6s^2 + 4r^2s^2}{r^3s(r-s)^2} + \frac{r^2 + 3rs + 6s^2 - 5r^2s^2}{2r^5s^3} \ln\left(\frac{1}{r^2}\right) \right. \\
& + \frac{10r^2 - 35r^4 + 10r^6 + 15rs + 45r^3s + 6s^2 - 17r^2s^2 - 2r^4s^2 + 16r^6s^2}{r^5(1-4r^2)(r-s)^3} \text{L}(r) \\
& \left. + \frac{-1 + 5s^2}{2s^3(-r+s)^3} \ln\left(\frac{r^2}{s^2}\right) + \frac{1 - 3s^2 - 4s^4}{s^3(-r+s)^3} \text{L}(s) \right]; \tag{A.54}
\end{aligned}$$

$$\begin{aligned}
P_1 = \frac{1}{3 m_\phi^4} & \left[ \frac{1}{s(r+s)} - \frac{1 + 2r^2}{2r^2(r+s)^2} \text{L}(r) + \frac{-2r + s}{4r^2s^3} \ln\left(\frac{1}{s^2}\right) \right. \\
& \left. - \frac{1}{4r^2(r+s)^2} \ln\left(\frac{r^2}{s^2}\right) + \frac{2r + 3s - 4rs^2 - 6s^3 + 8rs^4}{2s^3(r+s)^2(1-4s^2)} \text{L}(s) \right]; \tag{A.55}
\end{aligned}$$

$$\begin{aligned}
P_2 = \frac{1}{3 m_\phi^4} & \left[ -\frac{1}{r(r+s)} + \frac{-r + 2s}{4r^3s^2} \ln\left(\frac{1}{r^2}\right) + \frac{1 + 2s^2}{2s^2(r+s)^2} \text{L}(s) \right. \\
& \left. - \frac{1}{4s^2(r+s)^2} \ln\left(\frac{r^2}{s^2}\right) - \frac{3r - 6r^3 + 2s - 4r^2s + 8r^4s}{2r^3(r+s)^2(1-4r^2)} \text{L}(r) \right]; \tag{A.56}
\end{aligned}$$

$$\begin{aligned}
P_3 = \frac{1}{3 m_\phi^4} & \left[ -\frac{1}{s(r-s)} - \frac{1 + 2r^2}{2r^2(r-s)^2} \text{L}(r) + \frac{2r + s}{4r^2s^3} \ln\left(\frac{1}{s^2}\right) \right. \\
& \left. - \frac{1}{4r^2(r-s)^2} \ln\left(\frac{r^2}{s^2}\right) - \frac{2r - 3s - 4rs^2 + 6s^3 + 8rs^4}{2s^3(r-s)^2(1-4s^2)} \text{L}(s) \right]; \tag{A.57}
\end{aligned}$$

$$P_4 = \frac{1}{3m_\phi^4} \left[ \frac{1}{r(r-s)} + \frac{r+2s}{4r^3s^2} \ln\left(\frac{1}{r^2}\right) - \frac{1+2s^2}{2s^2(-r+s)^2} L(s) \right. \\ \left. + \frac{1}{4s^2(r-s)^2} \ln\left(\frac{r^2}{s^2}\right) + \frac{3r-6r^3-2s+4r^2s-8r^4s}{2r^3(r-s)^2(1-4r^2)} L(r) \right]; \quad (\text{A.58})$$

$$R_1 = \frac{1}{m_\phi^2} \left[ -\frac{1}{r^2} - \frac{-1+r^2}{2r^4} \ln\left(\frac{1}{r^2}\right) - \frac{1-3r^2}{r^4(1-4r^2)} L(r) \right]; \quad (\text{A.59})$$

$$S_1 = \frac{1}{m_\phi^2} \left[ -\frac{1}{s^2} - \frac{-1+s^2}{2s^4} \ln\left(\frac{1}{s^2}\right) - \frac{1-3s^2}{s^4(1-4s^2)} L(s) \right]. \quad (\text{A.60})$$

The functions appearing in the evaluation of the (crossed) box diagrams are again invariant under a simultaneous sign change of both arguments. In addition, they are pairwise related:  $N_5(r, s) = N_1(-r, s)$ ,  $N_6(r, s) = -N_2(-r, s)$ ,  $N_7(r, s) = N_3(-r, s)$ ,  $N_8(r, s) = N_4(-r, s)$ ,  $P_3(r, s) = P_1(-r, s)$  and  $P_4(r, s) = -P_2(-r, s)$ .

We also again provide the **massless quark limits of the loop functions**. Since  $N_3$ ,  $N_7$ ,  $P_1$  and  $P_3$  get multiplied with  $1/m_q$ , we keep terms up to linear in  $r$  in these functions:

$$P_1, P_3 \xrightarrow{r \rightarrow 0} \frac{1}{2m_\phi^4} \left[ \frac{1}{s^2} - \frac{1}{2s^4} \ln\left(\frac{1}{s^2}\right) + \frac{1-2s^2}{s^4} L(s) \right] \\ \pm \frac{r}{3sm_\phi^4} \left[ -\frac{2}{s^2} + \frac{1}{s^4} \ln\left(\frac{1}{s^2}\right) + \frac{4s^4+4s^2-2}{s^4(1-4s^2)} L(s) \right]; \quad (\text{A.61})$$

$$P_2, -P_4 \xrightarrow{r \rightarrow 0} \frac{1}{6m_\phi^4} \left[ \frac{1}{s^2} - \frac{1}{2s^4} \ln\left(\frac{1}{s^2}\right) + \frac{1+2s^2}{s^4} L(s) \right]; \quad (\text{A.62})$$

$$N_1, N_5 \xrightarrow{r \rightarrow 0} -\frac{1}{6m_\phi^4} \left[ \frac{1}{s^2} - \frac{1-3s^2}{2s^4} \ln\left(\frac{1}{s^2}\right) + \frac{1-s^2}{s^4} L(s) \right]; \quad (\text{A.63})$$

$$N_2, -N_6 \xrightarrow{r \rightarrow 0} \frac{1}{6m_\phi^4} \left[ \frac{1}{s^4} - \frac{3}{2s^2} + \frac{-1+3s^2}{2s^6} \ln\left(\frac{1}{s^2}\right) + \frac{1-s^2}{s^6} L(s) \right]; \quad (\text{A.64})$$

$$N_3, N_7 \xrightarrow{r \rightarrow 0} \frac{1}{3m_\phi^4} \left[ \frac{2}{s^4} + \frac{3s^2-2}{2s^6} \ln\left(\frac{1}{s^2}\right) + \frac{2-7s^2+2s^4}{s^6(1-4s^2)} L(s) \right] \\ \mp \frac{r}{2s^3m_\phi^4} \left[ 1 - \frac{2}{s^2} - \frac{2s^2-1}{s^4} \ln\left(\frac{1}{s^2}\right) - \frac{2}{s^4} \left( \frac{1-4s^2+2s^4}{1-4s^2} \right) L(s) \right]; \quad (\text{A.65})$$

$$N_4, N_8 \xrightarrow{r \rightarrow 0} \frac{1}{15m_\phi^4} \left[ \frac{1}{s^4} - \frac{7}{2s^2} - \frac{1-5s^2}{2s^6} \ln\left(\frac{1}{s^2}\right) + \frac{1-3s^2-4s^4}{s^6} L(s) \right]; \quad (\text{A.66})$$

$$R_1 \xrightarrow{r \rightarrow 0} \frac{1}{2m_\phi^2}. \quad (\text{A.67})$$

In eq.(A.61) the + sign in the second line refers to  $P_1$  and the - sign to  $P_3$ ; similarly, in the second line of eq.(A.65) the + sign refers to  $N_3$  and the - sign to  $N_7$ .

## B 2-Loop Calculations

In this appendix we provide details of the calculation of the two-loop diagrams contributing to the neutron EDM.

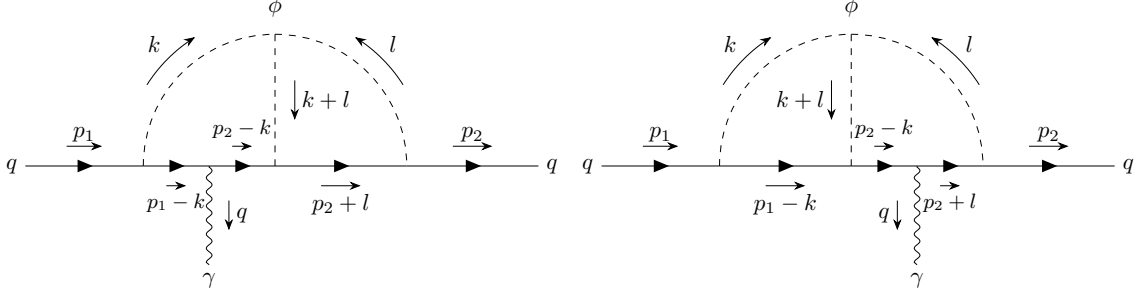


**Figure 17:** Two-loop Feynman diagrams generating quark EDMs and color-EDMs in Model I and IIa.

The matrix elements for diagram 1 (left) and diagram 2 (right) of Fig.17 generating EDMs in Model I and IIa can be written as:

$$i\mathcal{M}_1 = -\frac{i}{(16\pi^2)^2} 2eQ_q (h_2^q)^3 \mu_1 m_\phi \epsilon_\mu^*(q) [u(p_2) \mathcal{X}^\mu \gamma^5 u(p_1)] ; \quad (\text{B.1})$$

$$i\mathcal{M}_2 = -\frac{i}{(16\pi^2)^2} 2eQ_q (h_2^q)^3 \mu_1 m_\phi \epsilon_\mu^*(q) [u(p_2) \mathcal{Y}^\mu \gamma^5 u(p_1)] . \quad (\text{B.2})$$

Here  $Q_q$  is the electric charge of the quark and the loop functions  $\mathcal{X}^\mu = \sum_i^4 \mathcal{X}_i^\mu$  and  $\mathcal{Y}^\mu = \sum_i^4 \mathcal{Y}_i^\mu$  are described below.

$$\mathcal{X}_1^\mu = \int_X \frac{-2x_1}{\xi^4} p_2^\mu (t_3 + x_1 z_1 t_1) \left[ \frac{-3}{\Delta'} + \frac{1}{\xi^2} \frac{2(p_1 \cdot p_2) t_2 (t_3 + x_1 z_1 t_1) + m_q^2 (t_2^2 + (t_3 + x_1 z_1 t_1)^2)}{\Delta'^2} \right] ; \quad (\text{B.3})$$

$$\mathcal{X}_2^\mu = \int_X \frac{2x_1}{\xi^2} p_2^\mu \left[ \frac{-1}{\Delta'} + \frac{2}{\xi^2} \frac{(t_2 (p_1 \cdot p_2) + m_q^2 (t_3 + x_1 z_1 t_1)) (t_3 + x_1 z_1 t_1)}{\Delta'^2} \right] ; \quad (\text{B.4})$$

$$\mathcal{X}_3^\mu = \int_X \frac{-2z_1 m_q^2}{\xi^4} \frac{(t_3 + x_1 z_1 t_1 - t_2)}{\Delta'^2} (t_2 p_1^\mu + (t_3 + x_1 z_1 t_1) p_2^\mu) ; \quad (\text{B.5})$$

$$\mathcal{X}_4^\mu = \int_X \frac{4z_1 m_q^2}{\xi^2} \frac{(t_3 + x_1 z_1 t_1)}{\Delta'^2} p_2^\mu . \quad (\text{B.6})$$

Here  $t_{1,2,3}$ ,  $x_1$  and  $z_1$  are the five Feynman parameters required to describe diagram 1. The five dimensional measure  $\int_X$  is

$$\int_X \equiv \int_0^1 dt_1 \int_0^{1-t_1} dt_2 \int_0^{1-t_1-t_2} dt_3 \int_0^1 dx_1 \int_0^{1-x_1} dz_1, \quad \xi = [1 - t_1(1 - x_1(1 - x_1))]^{1/2} . \quad (\text{B.7})$$

Finally, the denominator  $\Delta'$  is given by:

$$\Delta' = -m_\phi^2 (z_1 t_1 + t_2 + t_3 - 1) + z_1^2 m_q^2 t_1 + \left( \frac{x_1 z_1 p_2 t_1 + p_1 t_2 + p_2 t_3}{\xi} \right)^2 . \quad (\text{B.8})$$

The loop functions  $\mathcal{Y}_i^\mu$  for the second diagram are obtained by the following replacements of Feynman parameters in the  $\mathcal{X}_i^\mu$  in eqs.(B.3) to (B.6):  $t_1 \rightarrow u_1$ ,  $t_2 \rightarrow u_3$ ,  $t_3 \rightarrow u_2$ ,  $x_1 \rightarrow x_2$  and  $z_1 \rightarrow z_2$ , as well as the replacement  $p_2^\mu \leftrightarrow p_1^\mu$ . This yields:

$$\mathcal{Y}_1^\mu = \int_Y \frac{-2x_2}{\chi^4} p_1^\mu (u_2 + x_2 z_2 u_1) \left[ \frac{-3}{\Delta''} + \frac{1}{\chi^2} \frac{2(p_1 \cdot p_2) u_3 (u_2 + x_2 z_2 u_1) + m_q^2 (u_3^2 + (u_2 + x_2 z_2 u_1)^2)}{\Delta''^2} \right]; \quad (\text{B.9})$$

$$\mathcal{Y}_2^\mu = \int_Y \frac{2x_2}{\chi^2} p_1^\mu \left[ \frac{-1}{\Delta''} + \frac{2}{\chi^2} \frac{(u_3 (p_1 \cdot p_2) + m_q^2 (u_2 + x_2 z_2 u_1)) (u_2 + x_2 z_2 u_1)}{\Delta''^2} \right]; \quad (\text{B.10})$$

$$\mathcal{Y}_3^\mu = \int_Y \frac{2z_2 m_q^2}{\chi^4} \frac{(u_3 - x_2 z_2 u_1 - u_2)}{\Delta''^2} (u_3 p_2^\mu + (u_2 + x_2 z_2 u_1) p_1^\mu); \quad (\text{B.11})$$

$$\mathcal{Y}_4^\mu = \int_Y \frac{4z_2 m_q^2}{\chi^2} \frac{(u_2 + x_2 z_2 u_1)}{\Delta''^2} p_1^\mu. \quad (\text{B.12})$$

The integration measure  $\int_Y$  is

$$\int_Y \equiv \int_0^1 du_1 \int_0^{1-u_1} du_2 \int_0^{1-u_1-u_2} du_3 \int_0^1 dx_2 \int_0^{1-x_2} dz_2, \quad \chi = [1 - u_1(1 - x_2(1 - x_2))]^{1/2}, \quad (\text{B.13})$$

and the denominator  $\Delta''$  is given by

$$\Delta'' = -m_\phi^2 (z_2 u_1 + u_2 + u_3 - 1) + z_2^2 m_q^2 u_1 + \left( \frac{x_2 z_2 p_1 u_1 + p_1 u_2 + p_2 u_3}{\chi} \right)^2. \quad (\text{B.14})$$

The qEDM is given by the coefficient of the dimension  $-5$   $CP$ -odd term  $\bar{u}(p_2) i \sigma_{\mu\nu} q^\nu \gamma^5 u(p_1)$  in the limit of vanishing momentum transfer  $q^2 \rightarrow 0$ . The  $\gamma^5$ -version of the Gordon identity

$$\bar{u}(p_2) (p_1 + p_2)^\mu \gamma^5 u(p_1) = \bar{u}(p_2) i \sigma^{\mu\nu} q_\nu \gamma^5 u(p_1) \quad (\text{B.15})$$

converts the matrix elements (B.1) into a suitable form to extract the qEDM. To that end the loop functions  $X_i^\mu$  and  $Y_i^\mu$  need to be transformed such that they are symmetric in the external quark momenta  $p_1$  and  $p_2$ :

$$\mathcal{X}^\mu = [\mathcal{X}] (p_1 + p_2)^\mu + \{\mathcal{X}\} q^\mu, \quad (\text{B.16})$$

$$\mathcal{Y}^\mu = [\mathcal{Y}] (p_1 + p_2)^\mu + \{\mathcal{Y}\} q^\mu. \quad (\text{B.17})$$

The parts of the loop functions proportional to  $q^\mu$ , denoted by  $\{\mathcal{X}\}$  and  $\{\mathcal{Y}\}$  respectively, can be ignored once the external spinors are taken into account by virtue of the Ward identity. The qEDM generated by the two diagrams is finally given by

$$d_q = \frac{2 e Q_q (h_2^q)^3 \mu_1 m_\phi}{(16 \pi^2)^2} \lim_{q^2 \rightarrow 0} \left( [\mathcal{X}] + [\mathcal{Y}] \right), \quad (\text{B.18})$$

where

$$\begin{aligned} \lim_{q^2 \rightarrow 0} [\mathcal{X}] &= \frac{1}{2} \int_X -\frac{2z_1 m_q^2 (t_3 + x_1 z_1 t_1)^2 - t_2^2}{\xi^4 (\Delta'|_{q^2 \rightarrow 0})^2} + \frac{4z_1 m_q^2 t_3 + x_1 z_1 t_1}{\xi^2 (\Delta'|_{q^2 \rightarrow 0})^2} \\ &\quad - \frac{2x_1}{\xi^4} (t_3 + x_1 z_1 t_1) \left[ \frac{-3}{\Delta'|_{q^2 \rightarrow 0}} + \frac{m_q^2 (t_3 + t_2 + x_1 z_1 t_1)^2}{\xi^2 (\Delta'|_{q^2 \rightarrow 0})^2} \right] \\ &\quad + \frac{2x_1}{\xi^2} \left[ \frac{-1}{\Delta'|_{q^2 \rightarrow 0}} + \frac{2m_q^2 (t_3 + t_2 + x_1 z_1 t_1)(t_3 + x_1 z_1 t_1)}{\xi^2 (\Delta'|_{q^2 \rightarrow 0})^2} \right]; \end{aligned} \quad (\text{B.19})$$

$$\begin{aligned} \lim_{q^2 \rightarrow 0} [\mathcal{Y}] &= \frac{1}{2} \int_Y -\frac{2z_2 m_q^2 (u_2 + x_2 z_2 u_1)^2 - u_3^2}{\chi^4 (\Delta''|_{q^2 \rightarrow 0})^2} + \frac{4z_2 m_q^2 u_2 + x_2 z_2 u_1}{\chi^2 (\Delta''|_{q^2 \rightarrow 0})^2} \\ &\quad - \frac{2x_2}{\chi^4} (u_2 + x_2 z_2 u_1) \left[ \frac{-3}{\Delta''|_{q^2 \rightarrow 0}} + \frac{m_q^2 (u_3 + u_2 + x_2 z_2 u_1)^2}{\chi^2 (\Delta''|_{q^2 \rightarrow 0})^2} \right] \\ &\quad + \frac{2x_2}{\chi^2} \left[ \frac{-1}{\Delta''|_{q^2 \rightarrow 0}} + \frac{2m_q^2 (u_3 + u_2 + x_2 z_2 u_1)(u_2 + x_2 z_2 u_1)}{\chi^2 (\Delta''|_{q^2 \rightarrow 0})^2} \right]. \end{aligned} \quad (\text{B.20})$$

The limit  $q^2 \rightarrow 0$  implies  $p_1 \cdot p_2 \rightarrow m_q^2$ , hence the denominators simplify to

$$\Delta'|_{q^2 \rightarrow 0} \equiv \lim_{q^2 \rightarrow 0} \Delta' = -m_\phi^2 (z_1 t_1 + t_2 + t_3 - 1) + m_q^2 \left( z_1^2 t_1 + \frac{(t_2 + t_3 + x_1 z_1 t_1)^2}{\xi^2} \right); \quad (\text{B.21})$$

$$\Delta''|_{q^2 \rightarrow 0} \equiv \lim_{q^2 \rightarrow 0} \Delta'' = -m_\phi^2 (z_2 u_1 + u_2 + u_3 - 1) + m_q^2 \left( z_2^2 u_1 + \frac{(u_3 + u_2 + x_2 z_2 u_1)^2}{\chi^2} \right). \quad (\text{B.22})$$

## References

- [1] XENON collaboration, *Excess electronic recoil events in XENON1T*, *Phys. Rev. D* **102** (2020) 072004 [2006.09721].
- [2] XENON collaboration, *Dark Matter Search Results from a One Ton-Year Exposure of XENON1T*, *Phys. Rev. Lett.* **121** (2018) 111302 [1805.12562].
- [3] PANDAX-4T collaboration, *Dark Matter Search Results from the PandaX-4T Commissioning Run*, *Phys. Rev. Lett.* **127** (2021) 261802 [2107.13438].
- [4] LUX collaboration, *Results from a search for dark matter in the complete LUX exposure*, *Phys. Rev. Lett.* **118** (2017) 021303 [1608.07648].
- [5] LUX collaboration, *Limits on spin-dependent WIMP-nucleon cross section obtained from the complete LUX exposure*, *Phys. Rev. Lett.* **118** (2017) 251302 [1705.03380].
- [6] LZ collaboration, *First Dark Matter Search Results from the LUX-ZEPLIN (LZ) Experiment*, *Phys. Rev. Lett.* **131** (2023) 041002 [2207.03764].
- [7] DEAP collaboration, *Search for dark matter with a 231-day exposure of liquid argon using DEAP-3600 at SNOLAB*, *Phys. Rev. D* **100** (2019) 022004 [1902.04048].

- [8] SUPERCDMS collaboration, *Results from the Super Cryogenic Dark Matter Search Experiment at Soudan*, *Phys. Rev. Lett.* **120** (2018) 061802 [[1708.08869](#)].
- [9] DARKSIDE collaboration, *DarkSide-50 532-day Dark Matter Search with Low-Radioactivity Argon*, *Phys. Rev. D* **98** (2018) 102006 [[1802.07198](#)].
- [10] CRESST collaboration, *First results from the CRESST-III low-mass dark matter program*, *Phys. Rev. D* **100** (2019) 102002 [[1904.00498](#)].
- [11] NEWS-G collaboration, *First results from the NEWS-G direct dark matter search experiment at the LSM*, *Astropart. Phys.* **97** (2018) 54 [[1706.04934](#)].
- [12] DAMIC collaboration, *Results on low-mass weakly interacting massive particles from a 11 kg-day target exposure of DAMIC at SNOLAB*, *Phys. Rev. Lett.* **125** (2020) 241803 [[2007.15622](#)].
- [13] PICO collaboration, *Dark Matter Search Results from the Complete Exposure of the PICO-60 C<sub>3</sub>F<sub>8</sub> Bubble Chamber*, *Phys. Rev. D* **100** (2019) 022001 [[1902.04031](#)].
- [14] LZ collaboration, *First Constraints on WIMP-Nucleon Effective Field Theory Couplings in an Extended Energy Region From LUX-ZEPLIN*, [2312.02030](#).
- [15] PLANCK collaboration, *Planck 2018 results. VI. Cosmological parameters*, *Astron. Astrophys.* **641** (2020) A6 [[1807.06209](#)].
- [16] G. Bertone, D. Hooper and J. Silk, *Particle dark matter: Evidence, candidates and constraints*, *Phys. Rept.* **405** (2005) 279 [[hep-ph/0404175](#)].
- [17] J. Fan, M. Reece and L.-T. Wang, *Non-relativistic effective theory of dark matter direct detection*, *JCAP* **11** (2010) 042 [[1008.1591](#)].
- [18] A.L. Fitzpatrick, W. Haxton, E. Katz, N. Lubbers and Y. Xu, *The Effective Field Theory of Dark Matter Direct Detection*, *JCAP* **02** (2013) 004 [[1203.3542](#)].
- [19] A.L. Fitzpatrick, W. Haxton, E. Katz, N. Lubbers and Y. Xu, *Model Independent Direct Detection Analyses*, [1211.2818](#).
- [20] N. Anand, A.L. Fitzpatrick and W.C. Haxton, *Weakly interacting massive particle-nucleus elastic scattering response*, *Phys. Rev. C* **89** (2014) 065501 [[1308.6288](#)].
- [21] R. Catena, K. Fridell and M.B. Krauss, *Non-relativistic Effective Interactions of Spin 1 Dark Matter*, *JHEP* **08** (2019) 030 [[1907.02910](#)].
- [22] P. Gondolo, S. Kang, S. Scopel and G. Tomar, *Effective theory of nuclear scattering for a WIMP of arbitrary spin*, *Phys. Rev. D* **104** (2021) 063017 [[2008.05120](#)].
- [23] N. Bozorgnia, D.G. Cerdeño, A. Cheek and B. Penning, *Opening the energy window on direct dark matter detection*, *JCAP* **12** (2018) 013 [[1810.05576](#)].
- [24] XENON collaboration, *Effective field theory search for high-energy nuclear recoils using the XENON100 dark matter detector*, *Phys. Rev. D* **96** (2017) 042004 [[1705.02614](#)].
- [25] PANDAX-II collaboration, *PandaX-II Constraints on Spin-Dependent WIMP-Nucleon Effective Interactions*, *Phys. Lett. B* **792** (2019) 193 [[1807.01936](#)].
- [26] SUPERCDMS collaboration, *Dark matter effective field theory scattering in direct detection experiments*, *Phys. Rev. D* **91** (2015) 092004 [[1503.03379](#)].
- [27] CRESST collaboration, *Limits on Dark Matter Effective Field Theory Parameters with CRESST-II*, *Eur. Phys. J. C* **79** (2019) 43 [[1809.03753](#)].

- [28] DARKSIDE-50 collaboration, *Effective field theory interactions for liquid argon target in DarkSide-50 experiment*, *Phys. Rev. D* **101** (2020) 062002 [2002.07794].
- [29] LUX collaboration, *Effective field theory analysis of the first LUX dark matter search*, *Phys. Rev. D* **103** (2021) 122005 [2003.11141].
- [30] DEAP collaboration, *Constraints on dark matter-nucleon effective couplings in the presence of kinematically distinct halo substructures using the DEAP-3600 detector*, *Phys. Rev. D* **102** (2020) 082001 [2005.14667].
- [31] CDEX collaboration, *First experimental constraints on WIMP couplings in the effective field theory framework from CDEX*, *Sci. China Phys. Mech. Astron.* **64** (2021) 281011 [2007.15555].
- [32] LUX collaboration, *Constraints on effective field theory couplings using 311.2 days of LUX data*, *Phys. Rev. D* **104** (2021) 062005 [2102.06998].
- [33] SUPERCDMS collaboration, *Effective Field Theory Analysis of CDMSlite Run 2 Data*, 2205.11683.
- [34] R. Catena and P. Gondolo, *Global fits of the dark matter-nucleon effective interactions*, *JCAP* **09** (2014) 045 [1405.2637].
- [35] R. Catena, *Prospects for direct detection of dark matter in an effective theory approach*, *JCAP* **07** (2014) 055 [1406.0524].
- [36] R. Catena and P. Gondolo, *Global limits and interference patterns in dark matter direct detection*, *JCAP* **08** (2015) 022 [1504.06554].
- [37] H. Rogers, D.G. Cerdeno, P. Cushman, F. Livet and V. Mandic, *Multidimensional effective field theory analysis for direct detection of dark matter*, *Phys. Rev. D* **95** (2017) 082003 [1612.09038].
- [38] Z. Liu, Y. Su, Y.-L. Sming Tsai, B. Yu and Q. Yuan, *A combined analysis of PandaX, LUX, and XENON1T experiments within the framework of dark matter effective theory*, *JHEP* **11** (2017) 024 [1708.04630].
- [39] S. Kang, S. Scopel, G. Tomar and J.-H. Yoon, *Present and projected sensitivities of Dark Matter direct detection experiments to effective WIMP-nucleus couplings*, *Astropart. Phys.* **109** (2019) 50 [1805.06113].
- [40] N.P. Avis Kozar, P. Scott and A.C. Vincent, *A Global Fit of Non-Relativistic Effective Dark Matter Operators Including Solar Neutrinos*, 2310.15392.
- [41] G. Lüders, *On the equivalence of invariance under time reversal and under particle-antiparticle conjugation for relativistic field theories*, *Dan. Mat. Fys. Medd.* **28** (1954) 1.
- [42] W. Pauli, *Exclusion Principle, Lorentz Group, and reversal of space-time and charge*, *Niels Bohr and the Development of Physics*, W. Pauli (ed.) New York: Pergamon (1955) .
- [43] PARTICLE DATA GROUP collaboration, *Review of Particle Physics*, *PTEP* **2022** (2022) 083C01.
- [44] C. Abel et al., *Measurement of the Permanent Electric Dipole Moment of the Neutron*, *Phys. Rev. Lett.* **124** (2020) 081803 [2001.11966].
- [45] J.M. Pendlebury et al., *Revised experimental upper limit on the electric dipole moment of the neutron*, *Phys. Rev. D* **92** (2015) 092003 [1509.04411].

- [46] M. Burghoff et al., *An Improved Search for the Neutron Electric Dipole Moment*, in *Meeting of the APS Division of Particles and Fields*, 10, 2011 [[1110.1505](#)].
- [47] J.B. Dent, L.M. Krauss, J.L. Newstead and S. Sabharwal, *General analysis of direct dark matter detection: From microphysics to observational signatures*, *Phys. Rev. D* **92** (2015) 063515 [[1505.03117](#)].
- [48] F. Bishara, J. Brod, B. Grinstein and J. Zupan, *From quarks to nucleons in dark matter direct detection*, *JHEP* **11** (2017) 059 [[1707.06998](#)].
- [49] E. Del Nobile, *Complete Lorentz-to-Galileo dictionary for direct dark matter detection*, *Phys. Rev. D* **98** (2018) 123003 [[1806.01291](#)].
- [50] M. Drees and R. Mehra, *Neutron EDM constrains direct dark matter detection prospects*, *Phys. Lett. B* **799** (2019) 135039 [[1907.10075](#)].
- [51] G. Arcadi, M. Lindner, F.S. Queiroz, W. Rodejohann and S. Vogl, *Pseudoscalar Mediators: A WIMP model at the Neutrino Floor*, *JCAP* **03** (2018) 042 [[1711.02110](#)].
- [52] N.F. Bell, G. Busoni and I.W. Sanderson, *Loop Effects in Direct Detection*, *JCAP* **08** (2018) 017 [[1803.01574](#)].
- [53] T. Li, *Revisiting the direct detection of dark matter in simplified models*, *Phys. Lett. B* **782** (2018) 497 [[1804.02120](#)].
- [54] T. Abe, M. Fujiwara and J. Hisano, *Loop corrections to dark matter direct detection in a pseudoscalar mediator dark matter model*, *JHEP* **02** (2019) 028 [[1810.01039](#)].
- [55] F. Ertas and F. Kahlhoefer, *Loop-induced direct detection signatures from CP-violating scalar mediators*, *JHEP* **06** (2019) 052 [[1902.11070](#)].
- [56] E. Del Nobile, *The Theory of Direct Dark Matter Detection: A Guide to Computations*, [2104.12785](#).
- [57] G. Jungman, M. Kamionkowski and K. Griest, *Supersymmetric dark matter*, *Phys. Rept.* **267** (1996) 195 [[hep-ph/9506380](#)].
- [58] M.A. Shifman, A.I. Vainshtein and V.I. Zakharov, *Remarks on Higgs Boson Interactions with Nucleons*, *Phys. Lett. B* **78** (1978) 443.
- [59] T. Bhattacharya, V. Cirigliano, R. Gupta, H.-W. Lin and B. Yoon, *Neutron Electric Dipole Moment and Tensor Charges from Lattice QCD*, *Phys. Rev. Lett.* **115** (2015) 212002 [[1506.04196](#)].
- [60] PNDME collaboration, *Iso-vector and Iso-scalar Tensor Charges of the Nucleon from Lattice QCD*, *Phys. Rev. D* **92** (2015) 094511 [[1506.06411](#)].
- [61] R. Gupta, B. Yoon, T. Bhattacharya, V. Cirigliano, Y.-C. Jang and H.-W. Lin, *Flavor diagonal tensor charges of the nucleon from (2+1+1)-flavor lattice QCD*, *Phys. Rev. D* **98** (2018) 091501 [[1808.07597](#)].
- [62] JLQCD collaboration, *Nucleon charges with dynamical overlap fermions*, *Phys. Rev. D* **98** (2018) 054516 [[1805.10507](#)].
- [63] C. Alexandrou et al., *Nucleon scalar and tensor charges using lattice QCD simulations at the physical value of the pion mass*, *Phys. Rev. D* **95** (2017) 114514 [[1703.08788](#)].
- [64] M. Pospelov and A. Ritz, *Neutron EDM from electric and chromoelectric dipole moments of quarks*, *Phys. Rev. D* **63** (2001) 073015 [[hep-ph/0010037](#)].



- [65] J. Hisano, J.Y. Lee, N. Nagata and Y. Shimizu, *Reevaluation of Neutron Electric Dipole Moment with QCD Sum Rules*, *Phys. Rev. D* **85** (2012) 114044 [[1204.2653](#)].
- [66] K. Fuyuto, J. Hisano and N. Nagata, *Neutron electric dipole moment induced by strangeness revisited*, *Phys. Rev. D* **87** (2013) 054018 [[1211.5228](#)].
- [67] T. Hahn, *CUBA: A Library for multidimensional numerical integration*, *Comput. Phys. Commun.* **168** (2005) 78 [[hep-ph/0404043](#)].
- [68] J.B. Dent, B. Dutta, J.L. Newstead and L.E. Strigari, *Effective field theory treatment of the neutrino background in direct dark matter detection experiments*, *Phys. Rev. D* **93** (2016) 075018 [[1602.05300](#)].
- [69] Y. Ema, T. Gao and M. Pospelov, *Reevaluation of heavy-fermion-induced electron EDM at three loops*, *Phys. Lett. B* **835** (2022) 137496 [[2207.01679](#)].
- [70] N. Yamanaka and E. Hiyama, *Weinberg operator contribution to the nucleon electric dipole moment in the quark model*, *Phys. Rev. D* **103** (2021) 035023 [[2011.02531](#)].
- [71] J. Ellis, *TikZ-Feynman: Feynman diagrams with TikZ*, *Comput. Phys. Commun.* **210** (2017) 103 [[1601.05437](#)].
- [72] H.H. Patel, *Package-X 2.0: A Mathematica package for the analytic calculation of one-loop integrals*, *Comput. Phys. Commun.* **218** (2017) 66 [[1612.00009](#)].